

## ABSTRACT

Title: DEVELOPMENT OF AN OFF-LINE RAINFLOW COUNTING  
ALGORITHM WITH TEMPORAL PARAMETERS AND DATA  
REDUCTION

James M. Twomey, 2016

Directed by: George E. Dieter Professor, Michael G. Pecht,  
Department of Mechanical Engineering

Rainflow counting methods convert a complex load time history into a set of load reversals for use in fatigue damage modeling. Rainflow counting methods were originally developed to assess fatigue damage associated with mechanical cycling where creep of the material under load was not considered to be a significant contributor to failure. However, creep is a significant factor in some cyclic loading cases such as solder interconnects under temperature cycling. In this case, fatigue life models require the dwell time to account for stress relaxation and creep.

This study develops a new version of the multi-parameter rainflow counting algorithm that provides a range-based dwell time estimation for use with time-dependent fatigue damage models. To show the applicability, the method is used to calculate the

life of solder joints under a complex thermal cycling regime and is verified by experimental testing.

An additional algorithm is developed in this study to provide data reduction in the results of the rainflow counting. This algorithm uses a damage model and a statistical test to determine which of the resultant cycles are statistically insignificant to a given confidence level. This makes the resulting data file to be smaller, and for a simplified load history to be reconstructed.

DEVELOPMENT OF AN OFF-LINE RAINFLOW COUNTING ALGORITHM WITH  
TEMPORAL PARAMETERS AND DATA REDUCTION

By

James M .Twomey

Thesis submitted to the Faculty of the Graduate School of the  
University of Maryland, College Park in partial fulfillment  
Of the requirements for the degree of  
Master of Science

2016

Advisory Committee:  
Professor Michael G. Pecht, Chair  
Professor Abhijit Dasgupta  
Doctor Diganta Das  
Doctor Michael D. Osterman

© Copyright by  
James M. Twomey  
2016

## Acknowledgements

I wish to express my thanks to all who have supported this work. I thank Dr. Michael Osterman and Prof. Michael Pecht for providing advice and direction to this project and for the work they put into reviewing my papers and software. Additionally, I am thankful to the rest of the CALCE staff and students for the helpful comments and suggestions they provided along the way, including Dr. Diganta Das, Prof. Abhijit Dasgupta, Dr. Michael Azarian, and Dr. Carlos Morillo along with the rest of the morning meeting group. Finally, I would like to express my gratitude for the support and encouragement of my girlfriend, An Thai; my sister, Prof. Kelly Sanders; and my parents, Matthew and Mary Twomey.

# Contents

|   |    |
|---|----|
| Chapter 1: Rainflow Counting .....                    | 1  |
| 1.1 Damage Modeling.....                              | 6  |
| 1.2 Damage Summation.....                             | 8  |
| 1.3 Probabilistic Modeling .....                      | 9  |
| 1.4 Overview of Thesis .....                          | 14 |
| Chapter 2: Literature Review .....                    | 14 |
| 2.1: Multi-parameter Rainflow Algorithms .....        | 14 |
| 2.2: Data Minimization .....                          | 18 |
| 2.2.1 Minimizing the Original Time History .....      | 18 |
| 2.2.2 Low-pass filters.....                           | 19 |
| 2.2.3 Range threshold filtering .....                 | 21 |
| 2.2.4 Damage exponent based reduction.....            | 22 |
| 2.2.5 Damage estimate reduction-based reduction ..... | 23 |
| 2.2.6 Binning .....                                   | 23 |
| Chapter 3: New Multi-parameter Rainflow Counting..... | 24 |
| 3.1 Proposed Algorithm .....                          | 26 |
| 3.2 Comparison to prior methods .....                 | 37 |
| 3.2.1 Comparison of Dwell Estimates .....             | 46 |
| 3.2.1 Comparison of Damage Estimates.....             | 53 |

|   |    |
|---|----|
| 3.3 Stability of Damage Estimates in the Proposed Algorithm.....  | 58 |
| 3.4 Stability over sampling rates .....   | 59 |
| 3.5 Stability over history length .....   | 61 |
| 3.6 Comparison of Run times and Memory Requirements.....  | 63 |
| Chapter 4: Automated Cycle Reduction .....  | 64 |
| 4.1 Proposed Algorithm .....  | 65 |
| 4.2 History Reconstruction.....   | 67 |
| 4.3 Demonstration of Automated Cycle Reduction and Reconstruction .....   | 69 |
| 5. Conclusions .....  | 72 |
| 4.1 Contributions .....   | 73 |
| A multi-parameter rainflow counting algorithm was developed and implemented to estimate dwell time using monotonic data and retain cycle timestamps. .... | 73 |
| 4.2 Suggested Future Work.....  | 74 |
| Works Cited .....   | 75 |

## List of Tables

|   |    |
|---|----|
| Table 1: Average dwell values .....   | 41 |
| Table 2: Estimated Damage .....   | 44 |
| Table 3: Damage Comparisons between Cluff and prosed dwell definitions..... | 45 |
| Table 4: Damage estimates .....   | 59 |
| Table 5: Data reduction comparisons .....                                   | 72 |

## List of Figures

|   |    |
|---|----|
| Figure 1: Rearranging the time series data and extracting a cycle. Adapted from [2] .....                         | 2  |
| Figure 2: Closed loop extraction .....  | 4  |
| Figure 3: Stability of a Monte Carlo output.....  | 13 |
| Figure 4: Low pass filter on a time-temperature history .....   | 20 |
| Figure 5: Dwell time definition based on load range percentage.....   | 27 |
| Figure 6: Time removal illustration.....  | 30 |
| Figure 7: Flow chart for the proposed algorithm .....   | 33 |
| Figure 8: Detailed flowchart for the half cycle extraction step.....  | 34 |
| Figure 9: Detailed flowchart for the dwell time calculation step.....   | 35 |
| Figure 10: Detailed flowchart for the data deletion step .....  | 36 |
| Figure 11: Each of the four data sets under consideration.....  | 40 |
| Figure 12: Average normalized dwell times for test profile (top) and the three remaining estimates (bottom) ..... | 42 |
| Figure 13: Comparison to experimental data.....   | 44 |
| Figure 14: Normalized damage estimates.....   | 45 |
| Figure 15: Stability of average dwell time for proposed and Vichare methods for test profile data set.....        | 47 |
| Figure 16: Stability of average dwell time for proposed and Vichare methods for outdoor data set .....            | 48 |
| Figure 17: Distribution of dwell times for outdoor data set.....  | 49 |
| Figure 18: Stability of average dwell time for proposed and Vichare methods for laptop data set .....             | 50 |
| Figure 19: Distribution of dwell times for laptop data set .....  | 51 |

|   |    |
|---|----|
| Figure 20: Stability of average dwell time for proposed and Vichare methods for desktop data set .....          | 52 |
| Figure 21: Distributions of dwell estimates for desktop data set .....  | 53 |
| Figure 22: Damage comparisons for outdoor data set.....   | 55 |
| Figure 23: Damage estimates for laptop data set .....   | 56 |
| Figure 24: Damage estimates for desktop data set .....  | 57 |
| Figure 25: Stability of damage estimates for each data set.....   | 58 |
| Figure 26: Stability of damage estimate over decreasing sampling rates.....                                     | 61 |
| Figure 27: Stability of damage estimates over smaller history lengths .....                                     | 62 |
| Figure 28: Run time comparisons .....   | 64 |
| Figure 29: Memory usage comparisons.....  | 64 |
| Figure 30: Example of reconstructed history for outdoor data set (top) and test profile data set (bottom) ..... | 68 |
| Figure 31: Data reduction for outdoor data set .....  | 70 |
| Figure 32: Data reduction for laptop data set.....  | 70 |
| Figure 33: Data reduction for desktop data set .....  | 71 |

## Chapter 1: Rainflow Counting

Fatigue in materials is caused by cyclically varying mechanical stresses. These stresses may result from shock, vibration, thermal expansion coefficient mismatches between joined materials, or thermal gradients within a material. To predict the life of a component under fatigue, information about the load cycles (e.g., cyclic mean and amplitude of the load cycle) are needed as inputs to a fatigue life model (e.g., Basquin's law, Coffin-Manson, Engelmaier's model). This would assume that the load conditions are constant, e.g., the load is cycling with a fixed mean and amplitude. However, in field conditions, materials may experience loads in a more complex pattern than can be parameterized in a single cyclic mean and amplitude. Therefore, there is a need for a technique that transforms a complex load history to a format which can be input into fatigue models. This transformation is achieved through "cycle counting."

Cycle counting allows individual cycles to be extracted from a load history. Cycles can be analyzed individually and aggregated through a damage summation rule, such as Palmgren-Miner's rule. This rule assumes that the percentage of life consumed by a load can be simplified to the ratio of cycles experienced at that load to the number of cycles to failure at that load. This allows multiple types of loads to be linearly summed. When the sum reaches unity, a failure is predicted.

$$\sum_{i=1}^k \frac{n_i}{N_i} = 1 \quad (0.0)$$

The most popular cycle counting algorithm for fatigue analysis in metals is rainflow counting [1]. This technique extracts intermediate cycles from larger half-cycles

in an irregular load history. To begin a simple rainflow counting algorithm [2], the time series load data first needs to be rearranged so that the history begins with either the highest peak or the lowest valley. This makes the assumption that the load history can be approximated as periodically repeating, as the end of the first history will be joined to the start of the second history.

Next, consider the two load ranges formed by the next three local extrema. If the first of these ranges is larger or equal to the second, the extraction criterion is met. If the point under consideration is not the first point in the history, discard the second range and count one cycle. If it is the first point in the history, delete that point and count one half cycle. Else, if the extraction criterion is not met, move forward in the time series to the

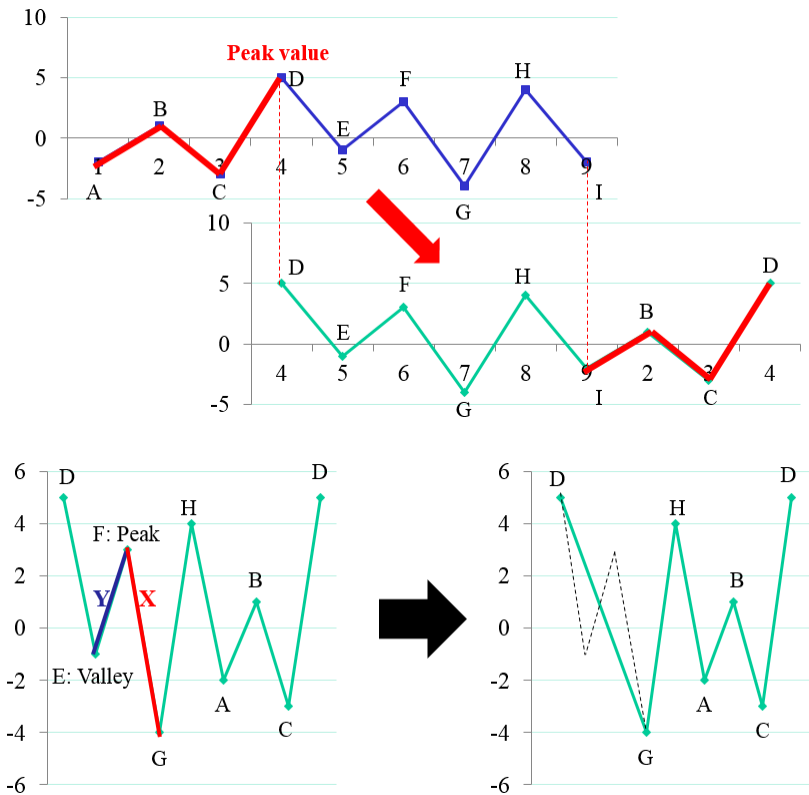
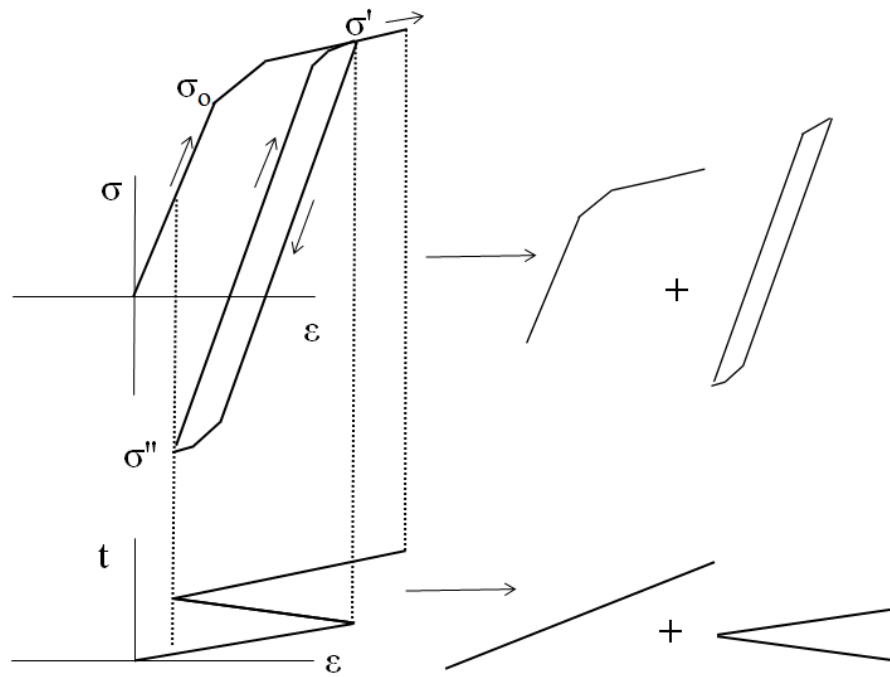


Figure 1: Rearranging the time series data and extracting a cycle. Adapted from [2]

next two load ranges, repeating until there is no more data or there is less than three peaks or valleys left. This process is partially illustrated above in Figure 1.

This is a three-point rainflow algorithm, since the two ranges considered are formed from three points. A four-point version of the algorithm can also be used [3] (where the extraction criteria requires that the middle of three ranges are less than or equal to the first and third), but this was proved to be equivalent to the three-point version [4]. This is also an offline algorithm requiring the entire history to be known before processing, although online versions have been proposed [5] [6].

There are other methods of cycle counting, including level-crossing counting, peak counting, simple-range counting, and range-pair counting [2]. Level crossing counting records every time a load crosses a defined threshold away from the neutral axis (i.e., an increasing positive load or a decreasing negative load). These crossings are assumed to be accompanied by corresponding load crossings towards the neutral axis. These crossings could be equivalently counted instead. This can be used to reconstruct full load cycles in a form useable for a damage model. Peak counting involves counting each maximum and minimum in the data, then matching the peaks in order of largest formed ranges to smallest. These matched peaks form individual cycles. Simple range counting divides the load histories into half cycles at each local extrema, so the damage modeling is simply applied to each half cycle.



**Figure 2: Closed loop extraction**

Rainflow counting is justified by assuming that closed loops in stress-strain space can be analyzed independently [1]. For example, in Figure 2, the load time series history experiences two load reversals. As shown on the stress-strain plot, the material deforms in a linear elastic fashion the stress reaches yield stress  $\sigma_o$ . After yielding, there is non-linear plastic deformation until the stress reaches the load reversal at  $\sigma'$ . The material then unloads linearly up to a total stress range of  $2\sigma_o$  (assuming this material exhibits kinematic hardening behavior) before deforming plastically. At the next load reversal  $\sigma''$  the loading path is again linear elastic to a total stress range of  $2\sigma_o$ . In the following plastic deformation, the load path intersects the original curve at  $\sigma'$ . This loop-closing behavior is known as the “memory effect.” Since this intersection forms a closed loop, the loops are treated as independent. The inside loop is extracted during rainflow counting and the larger loop is treated as continuous.

In one-parameter rainflow counting, only the ranges of the extracted cycles are counted. In many cases, engineers may be interested in other parameters in addition to load range. If a fatigue model also requires the mean of the cyclic load, the cycles are binned into a matrix to record both the mean and the range of the load cycles. For situations where the material experiences time-dependent damage mechanisms such as creep or oxidation, the rainflow algorithm must also record temporal information (e.g., ramp rate, cycle period, dwell time). Three-parameter rainflow counting extracts range, mean, and a temporal parameter such as dwell time.

When using rainflow counting for damage estimation on solder interconnects, three-parameter rainflow must be used. This is because solder experiences significant creep damage even at room temperature, so factors such as ramp rates and dwell times can impact damage accumulation.

Thermal cycling can cause damage to solder interconnects in electronics as a result of differing coefficients of thermal expansion (CTE) between an electronic component (e.g., an integrated circuit) and the supporting printed wiring board (PWB) to which it is soldered. These differing expansion rates cause shearing of the solder joints during a thermal cycle, eventually leading to cracks propagating through the joints, causing increases in electrical resistance across the connection or electrical opens. Specification and life prediction for these types of failures often involve the characterization of a usage profile involving one type of thermal cycle continually repeated. For example, the IPC Guidelines for Accelerated Reliability Testing of Surface Mount Solder Attachments [7] characterizes use environments as having a single maximum temperature swing (although it does caution that actual use conditions “need to

be established by thermal analysis or measurement”). In reality, temperatures will fluctuate irregularly, preventing the direct application of a fatigue life model (e.g., Engelmaier’s model).

## 1.1 Damage Modeling

Several models are available for estimating the life of solder interconnects during thermal cycling. One semi-empirical model was initially developed in 1983 [8]. This model was derived from the Coffin-Manson relationship with empirical corrections for factors such as temperature, cycle frequency, and lead stiffness. The strain range term in the original Coffin-Manson equation is replaced by an equation including temperature cycle range. This model was eventually included into standards such as the IPC Guide for Accelerated Testing of Surface Mount Assemblies (IPC-SM-785) [7], the IPC Design Guidelines for Reliable Surface Mount Technology Printed Board Assemblies (IPC-D-279) [9], and the IPC Design Guide for Performance Test Methods and Qualification Requirements for Surface Mount Solder Attachments (IPC-9701).

This model defines cycles to failure,  $N_f$ , as:

$$N_f = \frac{1}{2} \left( \frac{\Delta\gamma}{2\varepsilon'_f} \right)^{\frac{1}{c}} \quad (0.1)$$

In this equation,  $\varepsilon'_f$  is the fatigue ductility coefficient,  $\Delta\gamma$  is the cyclic shear strain range, and  $c$  is the fatigue plasticity exponent given by:

$$c = c_0 + c_1 T_{sj} + c_2 \ln\left(1 + \frac{360}{t_{dwell}}\right) \quad (0.2)$$

$T_{sj}$  is the mean solder joint temperature, and  $t_{dwell}$  is the average dwell time at each extreme.  $c_0$ ,  $c_1$ , and  $c_2$  are model coefficients. These three model coefficients, along with  $\varepsilon'_f$ , are calibrated for a particular solder material. The cyclic shear range for a leadless component is given by:

$$\Delta\gamma = \frac{FL_d\Delta\alpha\Delta T}{h} \quad (0.3)$$

$F$  is an empirical “non-ideal” factor that attempts to account for second order effects. This factor is dependent on the package type under consideration. For example, a CLCC package typically has a reported  $F$  value between 0.7 and 1.2 [10].  $L_d$  is the longest distance to the neutral point of expansion.  $\Delta\alpha$  is the difference in the coefficients of thermal expansion between the component and the substrate.  $\Delta T$  is the cyclic temperature range, and  $h$  is the solder joint height. For leaded parts, the cyclic shear range is:

$$\Delta\gamma = \frac{FDL_d\Delta\alpha\Delta T}{h} \quad (0.3)$$

$D$  is the lead displacement transmissibility [11], which accounts for lead stiffness.

There are several known caveats to using this model. First, it makes assumptions about solder joints. Short solder joints have properties driven more by their intermetallic formations rather than their solder [12]. It is also assumed that the solder joints are not influenced by things such as underfill or corner staking, which can alter the stresses experienced by the joints. Another caveat is with regard to local CTE mismatches. The Engelmaier model considers global CTE mismatches, i.e., between the package and the substrate that the solder provides a connection to. There is also a local mismatch between the solder and the component as well as between the solder and the substrate. This is a

large concern when the global CTE mismatch is very small, such as when a ceramic chip is mounted on a ceramic substrate. This may also cause issues in severe use environments [13]. The next caveat is that the model is not intended for large temperature ranges. Engelmaier [13] suggested that the model should not be used for temperature ranges that cross the region from  $-20$  to  $20^{\circ}\text{C}$ , because the damage mechanisms shift. Evans [14] suggests that the model is most appropriately used in a range of  $0\pm 100^{\circ}\text{C}$ . An additional caveat is a limitation on cycle frequency. At high frequencies where cycle times are less than 2 seconds or with dwells less than 1 second, creep and stress relaxation damage will be overestimated. Engelmaier suggests the direct application of Coffin-Manson in this case [13]. The last commonly reported caveat is that the model does not address leaded parts with high stiffness and large expansion mismatches [7]. This results in unexpected levels of plastic deformation, which degrades the model's predictions.

## **1.2 Damage Summation**

After the damage resulting from individual extracted cycles is determined, a mechanism is needed that can sum this damage. The most popular tool for this task is the Palmgren-Miner rule, also known as Miner's rule. Miner's rule is a linear damage summation rule often applied to fatigue analysis under variable amplitude loading conditions. The advantages of this rule include its ease of use, while the disadvantages include its assumption of damage independence. In reality, materials may exhibit cyclic hardening or softening over the course of the damage history, thus impacting the damage accumulation rate. Additionally, harsh loads early in the damage history cause periodic overstrain and may also make the sample more susceptible to damage later in the history.

While this method can give a large spread in accuracy, more sophisticated damage summation rules require empirical data to calibrate.

### **1.3 Probabilistic Modeling**

When a model gives a single value as an output rather than a probability distribution, it is a deterministic prediction. However, this ignores uncertainty. Uncertainty in damage prediction can come from several sources. For example, uncertainty in damage prediction of solder joints could result from variations in geometry of the specimen in question (e.g., as a result of manufacturing variations or defects) [14] [15] or variations in material properties (e.g., as a result of microstructural evolution over the life of the test). There is also uncertainty in the representation of the original load history. In a recorded time series history, sources of uncertainty can include noise in sensor measurements or potential error resulting from the sampling rate. If this analysis is being used to inform a design, or being used for life prediction, there is uncertainty in the usage conditions. For example, the sample load history may not exactly match history experienced by the system in the field.

One way to attempt to quantify uncertainty is to perform a Monte Carlo simulation, treating all model inputs (geometry factors, materials factors, loads and model constants) as random variables. If probability distributions for each uncertain input parameter into a model can be estimated, the distributions can be randomly sampled. These samples can then be input into the model. This can be repeated until there are enough samples to characterize the output distribution. This way, the uncertainty in the modeling results is estimated.

The input distributions can be estimated using historical data. In the case of rainflow counting, cycles are extracted from the time series history which results in a data vector for each parameter, (i.e., cyclic mean, range, dwell time). These data vectors resulting from the rainflow counting can be used to estimate probability distributions [16]. There are parametric and non-parametric methods to estimate probability distributions based on historical data.

Parametric methods require fitting the data is fit to a known parametric distribution (e.g., normal, lognormal, or Weibull distributions). The suitability of this strategy depends on how closely the data matches the choice of distribution. If the underlying distribution being estimated is non-standard (e.g., multi-modal), there will be a bias in the estimation. Non-parametric methods include histograms and kernel density estimation. Histograms simply count occurrences of data points within a bin range, forming a discrete distribution. Kernel density estimation provides a smoothed estimation (compared to a histogram) by weighting the points (within a bandwidth  $h$ ) around each sample according to a parametric kernel function  $K$ .

$$\hat{f}_h(x) = \frac{1}{nh} \sum_{j=1}^n K\left(\frac{x-x_j}{h}\right) \quad (1.31)$$

Commonly used kernel functions include normal, uniform, triangular, and Epanechnikov. While the local weighting function for each point is parametric, the total probability distribution formed by the sum of the local functions is not, because the kernel function is simply being used as a smoothing function around samples rather than to structure the entire estimated distribution. If the parameter being estimated needs to be

bounded (e.g., if a parameter cannot be negative), the estimates near the boundaries may be biased. Corrections can be applied to alleviate this issue [17]. This can be a problem when estimating a parameter such as dwell time or cyclic range, since many samples may be within the kernel bandwidth of zero, but negative values of these parameters are impossible.

The suitability of a non-parametric estimation technique depends on how comprehensively the observed data characterizes the underlying distribution. In higher dimensions, non-parametric estimation techniques suffer from the curse of dimensionality, since sample data tends to be more sparse (i.e., under-sampled) in higher dimensional space. As a result of data sparsity, non-parametric estimations tend to have higher variances compared to parametric techniques.

In using histograms, a bin width must be selected to form the range into which data is counted. If the bin width is too large, the distribution is over-smoothed. In this case, the details of the underlying distribution are lost. If the bin width is too small, the distribution is under-smoothed. In this case, the noise in the data is over represented, distorting the estimation of the underlying distribution. The bin width should be optimized so that the histogram is neither under- nor over-smoothed. To calculate optimal bin width for normally distributed data, the Scott rule [18] can be used:

$$h_n^* = 3.49sn^{-1/3} \tag{1.32}$$

For non-Gaussian data, the Freedman-Diaconis rule [19] can be used:

$$h_n^* = 2(IQR)n^{-1/3} \tag{1.33}$$

The analog to bin width in kernel density estimation is bandwidth. This is the width from a data point where the distribution is weighted by the data point's kernel function.

Optimal bandwidth for kernel density estimation can be calculated with the following formula [16]:

$$h^{opt} = 1.06\hat{\sigma}n^{-\frac{1}{5}} \quad (1.34)$$

In order for the result of the Monte Carlo simulation to be realistic, correlations between input variables should be considered in order to only generate meaningful data samples [20]. For example, if cycles with at high temperatures only occur with small amplitudes, then a high temperature should not be sampled with a large amplitude during the same Monte Carlo iteration. This correlation can be modeled in several ways. A simple way to create a dependency structure is fitting a parametric model that treats a variable as a function of the variables it is correlated with (e.g., with a linear function). Other options include rank order correlation [21], standard normal transformation [22] and copulas [23] [24]. The optimal method depends on the data. In the thermal cycling profile used by Chai [25], the extracted parameters are rigidly correlated as a result of the limited number of cycle types in the profile. Therefore, sampling one variable (e.g., dwell time) and treating the others (e.g., mean temperature and temperature range) as dependent variables is adequate for simulating this history.

After each Monte Carlo iteration, the cumulative average output is calculated. When this value becomes stable as a function of iteration number, the simulation is complete (as illustrated in Figure 3). This stabilization can also be analyzed in terms of

the Standard Error ( $SE$ ) of the Mean formula, in terms of sample standard deviation  $\sigma$  and sample size  $n$ :

$$SE = \frac{\sigma}{\sqrt{n}} \quad (1.35)$$

The simulation can be stopped when the standard error reaches 1% of the mean (i.e.,  $SE \leq 0.01\mu$ ). The cumulative average output value should approximately match the deterministic model prediction, if one is available.

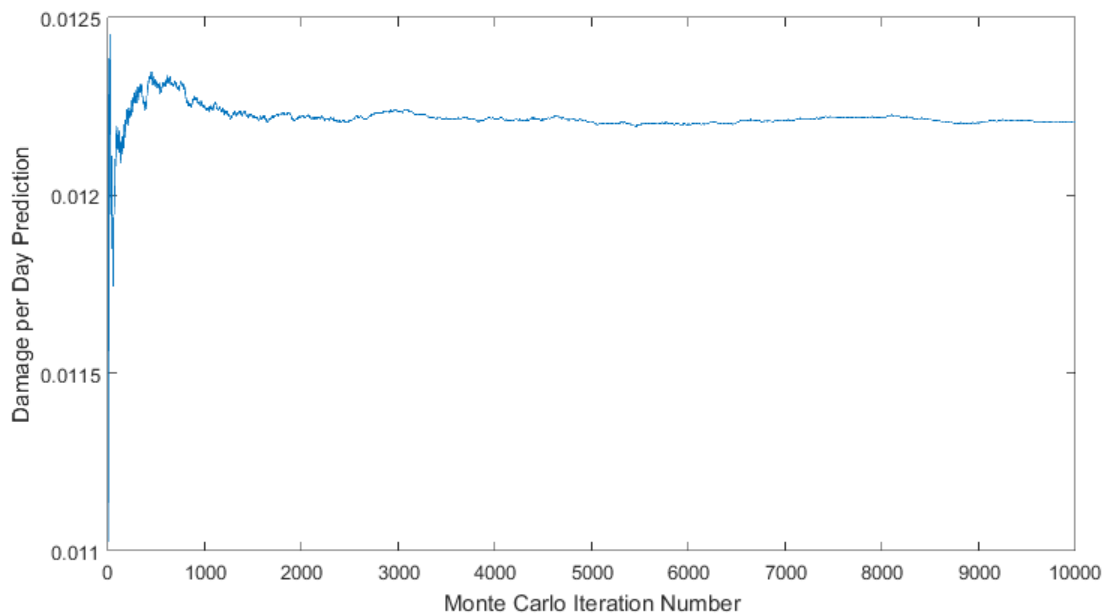


**Figure 3: Stability of a Monte Carlo output**

Rather than randomly sampling correlated distributions, other sampling methods can be used for a Monte Carlo analysis. In cases where the sampling probability depends entirely on the preceding state of the system, Markov chains can capture this dynamic that would otherwise be ignored by random sampling. Data which exhibits autocovariance can be modeled with an autoregressive (AR) model.

## **1.4 Overview of Thesis**

This thesis aims to develop a rainflow counting method which is sensitive to temporal parameters such as dwell time and cycle start time, as well as a data reduction method to reduce the file size of the results and allow for a simplified load history to be reconstructed. Chapter 1 provides an introduction into standard rainflow counting, a dwell-time sensitive fatigue damage model for solder interconnects, as an introduction to damage summation and probabilistic damage modeling. In chapter 2, the literature relevant to time-parameter sensitive rainflow counting, as well as data reduction techniques used with rainflow counting, is reviewed. Chapter 3 develops and analyzes the new version of rainflow counting which uses a load range-based definition of dwell time, in addition to extracting range, mean, and half-cycle start time. Chapter 4 develops and analyzes an automated data minimization strategy which reduces the size of the rainflow results using a damage model and a statistical test, allowing a unique simplified history to be reconstructed. The conclusions, contributions and suggested future work of this thesis are given in Chapter 5.

## **Chapter 2: Literature Review**

### **2.1: Multi-parameter Rainflow Algorithms**

When using rainflow counting for damage estimation on solder interconnects, three-parameter rainflow counting is used, because solder experiences time-dependent creep damage even at room temperature, and the ramp rates and dwell times can impact damage accumulation. Cluff [26] and Denk both [27] implemented a three-parameter

rainflow algorithm which recorded the half cycle period formed within the range under consideration.

Cluff's three parameter rainflow method first simplified the history into peaks and valleys. Next, cycles are under the same criteria as a standard 3-point rainflow method [2] (the range under consideration must be less than or equal to in magnitude to the preceding range). The peak temperature and the temperature range are discretized to 2°C intervals and recorded, and the dwell time is taken to be 50% of the half cycle time, regardless of the actual load path between the two points. The dwell was discretized to 12 minute intervals (based on the recording interval of the logging equipment). Therefore, a quarter of the assumed full cycle time would be counted as dwell time. Three passes of the algorithm were made before the remainder of the history was counted using simple range counting (i.e., counting half cycles sequentially). This algorithm recorded only full cycles, but during simple range counting, half cycles did not exactly match up. It was assumed that positive half cycles can be combined with the closest, but smaller, negative cycles" to be counted as a full cycle, then simply counting the remaining half cycles as full cycles. The justification for doing this is that both assumptions provide conservative estimates. Denk's algorithm used standard rainflow counting [2] along with recording the "heating time" of each cycle between the first and second extrema in the extracted cycle.

Both of these algorithms calculate the time elapsed during the extracted range, but record full cycles. An improvement would be to independently interpolate the time length of the second half of the cycle. Nagode [28] developed an online temperature-modified cycle counting algorithm. Amzallag's four-point algorithm [3] was modified to calculate

full cycle period by interpolating the end point of the second half of the cycle. However, no dwell time calculation was made.

A third strategy was implemented by Vichare [29], which used a supplementary algorithm to record dwell time independently from rainflow counting. While this does not allow a dwell time to be associated with a particular extracted cycle, it does allow for a probability distribution to be formed, which can be sampled in a Monte Carlo simulation. This strategy first uses a moving average filter to smooth noise, then the history is simplified into increasing, decreasing and dwell regions. The user chooses a threshold range and ramp rate to merge small-amplitude cycles and shallow sloped regions into dwell. Each the elapsed time and load for each dwell region is counted. After that, a four-point rainflow algorithm is used to extract cycles (their ranges and means). The thresholds were suggested to be calculated as a function of exponent in the damage model. The correlations between dwell time and dwell temperature is also recorded, in addition to the correlations between cyclic range and mean. With these sample populations extracted, probability distributions could be estimated using parametric or non-parametric (i.e., histograms or kernel density estimation) methods, for use in a Monte Carlo simulation. A problem with using this strategy is that it defines dwell differently than the other techniques discussed. The dwell time recorded is not the dwell time during a particular cycle. It is just a flat region in the data, without any inherent relationship with any cycle. This may be suitable if the damage model calculates damage from dwell loads independently from damage done by cyclic loading. However, if the model used (e.g., Engelmaier's model) requires a dwell time for each cycle, Vichare's method does not provide this parameter defined in this way. In addition to the fact that the dwells are not

related to any cycle, there is no inherent reason that the dwells and cycles are found in the history in equal quantities. In the event that there are more cycles extracted than dwells, the dwells would be over represented in the simulation if both distributions were sampled one-to-one. Therefore, when using a model which requires a dwell of a given cycle, this supplementary algorithm is unsuitable. An advantage of this strategy is that after analyzing (running both the supplementary algorithm and rainflow counting) a segment of a history, the results can be stored as distributions rather than lists of cycles, lowering data storage requirements.

One study [30] demonstrated the impact of different methods of cycle counting on the accuracy of damage prediction. An irregular thermal cycling profile comprising a large cycle with several minicycles at the upper range was developed, and then split into cycles four different ways, analyzing them with a semi-empirical damage accumulation model and a numerical damage accumulation model, and then compared the results with experimental data. Each of the cycling counting methods counted six minicycles of equal range, mean and period. The first cycle counting method cut the larger cycle's upper range to be at the low end of the minicycles. The second and third method had the upper end of the large cycle to be the middle and upper end of the minicycles, respectively. All three of the first three methods had the length and ramp rates of the larger cycle unchanged. The fourth cycle shortened the large cycle so that the upper end matched with the first minicycle before ramping down to the lower end of the complex cycle. None of these cycle counting methods matches rainflow counting, which would only count five minicycles. However, the suggestion of whether to shorten the length (in terms of time elapsed) of the larger range after cycle extraction was one previously unexplored. Chai

found the smallest modeling errors (compared to the experimental results) using the second cycle counting method, and the largest errors using the first cycle counting method. The relative errors were small enough that strong conclusions cannot be drawn as to whether changing the cycle time of the larger cycle leads to consistently higher or lower accuracies, since this may be a function of many other things beyond cycle counting method (such as cycling profile, package type, choice of models, etc.).

## **2.2: Data Minimization**

When monitoring environmental loads such as load cycles, it is advantageous to minimize the amount of data required to represent the load history. In the context of cycle counting for fatigue life prediction, data minimization strategies may be applied to the original time series history prior to cycle counting, or it may be applied after the cycle counting has already been applied. An ideal data minimization strategy should reduce storage and processing requirements without impacting the damage estimate.

### **2.2.1 Minimizing the Original Time History**

A simple way to reduce the amount of data storage required would be to reduce the sampling rate of the sensor system. If the load is slowly changing relative to the sampling rate, the data acquisition rate may be needlessly high. However, lowering the sample rate may cause details to be lost in the original time history that could turn out to be significant.

Another technique that can be applied as the original time series history is recorded is compression. This encodes the data into a smaller form than the original history, ideally without loss. While the compressed history would need to be decoded

before it can be used again, this would be useful in situations (such as sensor motes) where onboard data storage and computational power are limited. Compressing the size of the history would be advantageous for storage or during data transmission. A simple compression algorithm is run-length encoding, which compressed repeated values into a two-value tuple of the value and the number of consecutive occurrences of that value. This can lead to large reductions if the load values in this history tend to fall on one of several discrete levels, increasing the probability of consecutive readings.

A third technique that can be applied to reduce the number of data points representing the original history is a line fitting method. For example, if a load is changing linearly, then the points along the load between the ends of the linear region can be removed without detail, since linear change between data points would otherwise be assumed. This concept can be extended to removing points along approximately linear load paths, if the user defines an acceptable maximum deviation parameter. This is called the Ramer-Douglas-Peucker algorithm after the authors who independently invented it [31] [32]. A non-parametric version, where the maximum deviation does not need to be specified, was also developed [33].

### **2.2.2 Low-pass filters**

A low-pass filter removes small, high frequency signal oscillations while allowing longer-term fluctuations to be retained. This is an attractive technique in the case that the high frequency component of the signal in a particular application is considered to be noise (or otherwise irrelevant). In load monitoring applications, high frequency signals may simply be sensor noise. In fatigue life prediction in general, small amplitude cycles will tend to contribute a minority of the total damage (whether these small cycles are

generated by noise or if they are actually experienced by the monitored system). Examples of smoothing filters usable on a time-series load history include moving average (shown below in Figure 4), lowess, and Savitky-Golay. This technique contributes to data reduction because less cycles will be extracted during the cycle counting, decreasing the time required to perform the extraction and shortening the list of extracted cycles.

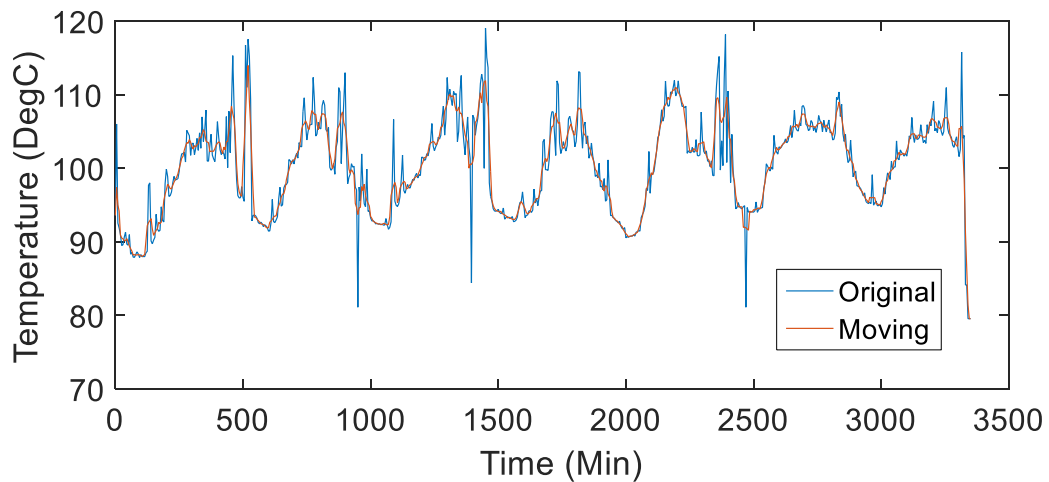


**Figure 4: Low pass filter on a time-temperature history**

Low-pass filters generally require an input parameter, such as the span of a moving average. This span defines how many data points are within the smoothing window. Higher spans will lead to more smoothing, at the risk of details being averaged out of the history. Low-pass filters work best when there is noise that is higher frequency and smaller in amplitude than the signal. Histories with high sampling rates (relative to the rate of change of the signal) tend to be better candidates than those with smaller sampling rates, since the same span will include a larger amount of time. Vichare [29] explored using a moving average prior to rainflow counting, reasoning that high frequency noise would be averaged out without impacting the overall history. The span

(also called the smoothening parameter or smoothing parameter) was suggested to be the square root of the sampling frequency (in hertz) rounded to the nearest integer.

A problem with low-pass filters is that they inherently average out the peaks in the data, making damage estimates less conservative since extracted cyclic ranges are attenuated.

### **2.2.3 Range threshold filtering**

Range threshold filtering is a data reduction technique which eliminates cycles below a certain cycle amplitude. Cycles smaller than this are deemed to be irrelevant (e.g., they are an artifact of signal noise or that they cause a negligible amount of damage) and are eliminated.

One example of a range threshold filtering technique is “Ordered Overall Range” the user picks a “reversal elimination index”,  $S$ . This represents the ratio to the largest observed cycle to the threshold amplitude that is to be eliminated. Based on this value, the time series history is translated upwards  $S/2$  and downward  $S/2$ . Beginning at the start of the time series, a path is drawn to the first peak or valley of either of the higher or lower offset history (whichever occurs first). Then, the shortest possible path is drawn through the two offset histories. This forms a path from the beginning of the history to the end of the history. Whenever this path experiences a local extrema, the corresponding point in the original history is flagged. Finally, all of the points in the original history which are not flagged are discarded, successfully eliminating monotonic data as well as cycles smaller than the threshold. This reduction strategy has been used with rainflow counting [34], including three-parameter rainflow counting [26] [16]. This reduces the

number of points in the original history as well as the number of cycles extracted.

However, since the monotonic data is discarded, all the detail about load path between extrema is lost.

#### **2.2.4 Damage exponent based reduction**

Many fatigue damage models follow a power-law relationship with cycle amplitude (e.g., Basquin's law, Coffin-Manson relationship). Consequentially, this causes higher-amplitude cycles to cause a higher fraction of the total damage during a history than smaller cycles. This imbalance is more severe as the damage exponent increases. As a result of this relationship, a damage model with a larger damage exponent can tolerate a more aggressive small cycle elimination strategy (i.e., setting the range threshold comparatively higher than if the damage exponent were smaller) while keeping a similar damage prediction. Vichare [29] suggested that for damage models where the damage is proportional to the temperature range raised to an exponent,  $n$ , the threshold range can be chosen to be the  $n$ th root of the maximum temperature range measured. However, the trend of this rule is that for higher damage exponents, the threshold value remains more stable as the maximum observed range increases. This does not match with the observation that when damage exponents are higher, the larger cycles tend to dominate the percent of total damage more than for smaller damage exponents. Therefore, the threshold value should rise more quickly (as a function of increasing maximum range) when the damage exponent is higher, since more cycles can be removed without significantly impacting the damage estimation. This strategy also cannot be used in cases where the damage exponent is a function of cycle parameters. For example, in the Engelmaier's model, the exponent is partly a function of mean temperature and dwell

time, so there is no exponent to base a threshold on. This technique requires rainflow counting to have already been performed before data reduction can occur.

### **2.2.5 Damage estimate reduction-based reduction**

Choosing a range threshold prior to cycle extraction does not take into account cycle frequency. While fatigue damage tends to be dominated by large cycles, in many cases the smaller cycles are much more frequent. It can occur that even though the smaller cycles individually contributes a minimal amount of damage to the total, the frequent occurrence of these cycles make them more important than the larger cycles in total. If the results of the cycle counting are binned into a histogram, the damage per cycle can be multiplied by the frequency of that cycle to obtain the damage per cycle type. With this information, the engineer can choose an acceptable level of damage to remove when deciding which bins to remove. This technique requires rainflow counting to have already been performed, as well as the damage estimation per cycle type.

### **2.2.6 Binning**

Instead of storing the results of rainflow counting as a list of cycles, oftentimes the results are binned into a one dimensional or two dimensional histogram, depending on how many parameters are extracted (i.e., just the range or both the mean and range). As the number of parameters extracted during rainflow counting increases (e.g., if dwell is also extracted in addition to range in mean), the histograms will tend to become more sparse as a result of the curse of dimensionality. For example, if  $n$  cycles are extracted from a history, and only the range of each cycle is recorded, these ranges can be stored in a histogram  $m$  bins wide. Therefore, the average number of samples per bin is  $n/m$ . If the mean is also binned into a histogram  $m$  bins wide, the average number of samples per bin

is  $n/m^2$ . If dwell times are extracted beyond that, the average number of samples per bin becomes  $n/m^3$ , and so on. As a result, histograms will become less space efficient as their dimensionality rises, due to the number of zero-count bins that must be stored, and the diminishing likelihood that multiple cycles occur in the same bin (i.e., they have similar enough extracted cycle parameters in each binned dimension to be placed with another cycle). A more efficient structure in this case would be a sparse array, where a list of observed bins as well as the observed frequency is recorded, so that bins with no counts do not take up space.

Bin size can impact the representation of the data. Bins that are too small will lead to less data reduction, but will also over-represent the random variation in the population. If the histograms are intended to represent a probability distribution, this situation is referred to as “undersmoothing.” Conversely, if the bins are too large, too much detail is lost. This is called “oversmoothing.” Optimal binning rules have been developed to mitigate this [19] [18].

### **Chapter 3: New Multi-parameter Rainflow Counting**

Prior art versions of rainflow algorithms for extracting temporal parameters (e.g., dwell time or cycle period) have several shortcomings. First, current algorithms require the load history to be simplified into a sequence of peaks and valleys. However, this makes it impossible to accurately account for how the load varies between consecutive extrema. This can make a difference when calculating parameters such as dwell time or ramp rate. A hypothetical load half cycle which features long dwells at either extrema with a sharp ramp between them should not be treated the same as another half cycle

where the load varies linearly between the two extrema. However, if monotonic data is discarded, the difference between these two load paths is lost.

Current rainflow algorithms also discard cyclic sequence. If it assumed that damage cannot be summed linearly, this causes a problem. It is possible that material exhibits a sequential effect in fatigue damage accumulation. Materials can cyclically harden or soften over the course of their life. This can be accounted for in a non-linear damage model, where the cycles must be added in the sequence that the damage occurred. Therefore, if a rainflow counting algorithm records the sequence in which the cycles occurred in the original time series history, they can be summed non-linearly in the correct order.

It is also sometimes desirable to generate simplified load histories for testing purposes. This can be accomplished by applying a rainflow algorithm, discarding cycles contributing small amounts of damage, and then reconstructing the history based on the cycle list. If the original starting times of each half cycle was not recorded, this reverse transformation from the cycle list to a time series history could not be uniquely done. The engineer would need to choose where to place intermediate cycles onto larger cycles, rather than using their original time stamp.

Treatment of dwell time in the prior art has been inadequate. Since rainflow algorithms currently simply the load behavior to sequences of extrema, it is impossible to make a determination of dwell periods. Current methods, because of the removal of monotonic data, are forced to assume that dwell times are a fixed fraction of half cycle time, or they need to determine dwells prior to cycle counting. However, if dwells are

counted prior to cycle counting, the dwells are inherently not connected to any particular cycles. Therefore, this defines dwell differently than a damage model which requires a dwell for a particular cycle (e.g., Engelmaier's model), and it therefore not useful for such a model. It would be advantageous to develop a dwell estimation method which took load path (i.e., monotonic data within a cycle) into account for each individual cycle that is extracted.

### **3.1 Proposed Algorithm**

The dwell time is the time an element remains in a given state. For example, in an idealized load path, it is the time the test specimen remains at a given load level before ramping up or down. In a more flexible definition, the JEDEC standard for temperature cycling [35] defines soak time (i.e., dwell time) as a part of the cycle period occurring in a particular range of the extreme. Specifically, Therefore, it is the time where the load is within  $+15^{\circ}\text{C}$  to  $-5^{\circ}\text{C}$  of the maximum sample temperature specified by the profile or within  $-15^{\circ}\text{C}$  to  $+5^{\circ}\text{C}$  of the lower temperature specified by the profile. Therefore, since soak time (analogous to dwell time) is defined in terms of cyclic range, it is reasonable to calculate dwell time of a cycle based on the amount of time the load dwells within a user-defined fraction of the cyclic range. A hard number such as  $5^{\circ}\text{C}$  would not generalize well as maybe times cycles smaller than this range may be extracted. A fixed percentage could instead be used to define the dwell region, so that the time spent within this region towards either extreme of the half cycle is defined as dwell time. For example, the top and bottom 25% of the range can be defined as dwell regions (illustrated in Figure 5), and the dwell times can be calculated based on that definition. Since the 75% and 25% lines

will not necessarily fall on a particular data point, it is necessary to interpolate where the dwell regions begin and end.

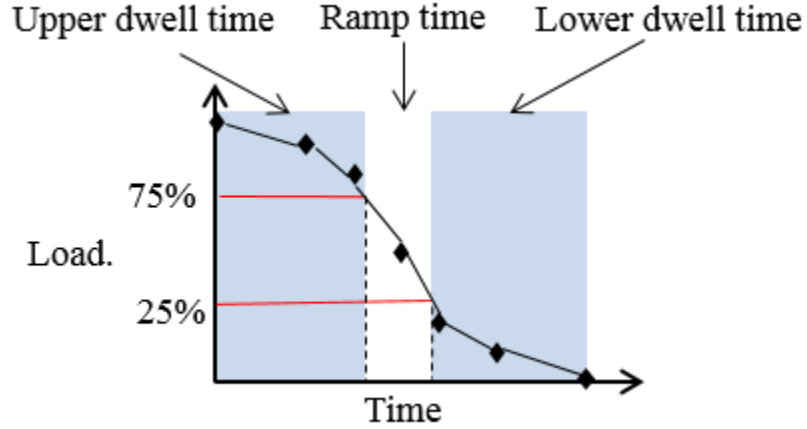


Figure 5: Dwell time definition based on load range percentage

The load range percentage may be chosen in order to make the estimate robust to small ramp ramps (which the engineer may assume is essentially dwell) or discretization error (where the load might have dwelled but the true load was not sampled fast enough to “catch” the flat regions.” Choosing a load range percentage  $N$  so that it is resilient to small slopes first involves choosing a threshold slope ( $\alpha_t$ ) below which ramps are insignificant. Choosing a threshold slope of zero classifies only strictly flat regions as dwell, and a threshold slope of 90 should classify the entire load path as dwell. Therefore, the following equation may be used:

$$N = \frac{\cos\alpha_t}{1.8} \quad (3.11)$$

In order to make the estimate robust to discretization error, the average number of half cycles extracted divided by the number of data points in the history should be calculated in order to find the average number of points per half cycle. If there is only

two points per half cycles, there is no load path information between extrema and the load range percentage  $N$  should be assumed to be half of the half cycle time (assuming that each cycle comprises an equally proportioned ramp up, an upper dwell, a ramp down, and a lower dwell). As the point density increases,  $N$  can be lowered since the possible discretization error lessens. Therefore, the following equation can be used:

$$N = \frac{100}{4\left(\left(\frac{N_p}{N_c}\right)-1\right)} \quad (3.12)$$

The maximum between these two equations can be used as the load range percentage.

When a cycle is extracted (using a standard extraction criteria [2]), the half cycle time of the first of the two independently treated half cycles can be simply calculated as the difference between the two data points in the time dimension. The end of the second half cycle may need to be interpolated if that does not fall on a data point. If the beginning or end extreme of a half cycle falls on a “flat peak” (i.e., multiple points at the same load consecutively), the middle point can be used. Next the load thresholds are calculated based off the user-chosen range-threshold parameter (e.g., 25%), and the point where the half cycles cross these thresholds (two thresholds per half cycle) is interpolated.

Another two parameters which can be extracted are the start times of each half cycle. This is valuable in order to enable non-linear damage summation, in case each thermal cycle must be summed in the same order to model load-sequence effects. It also allows the used to reconstruct the original time-temperature history by mapping the

extracted cycle list to locations in time in the original history. A third thing that is enabled by recording the start times of each half cycle, is the conversion of the damage vs. number of cycles history typically reported for fatigue damage to a damage vs. time. Since the half cycle start time and duration is known, and the damage per half cycle can be calculated, the damage spread out over the cycle duration could be superposed onto a time series at the correct time to estimate a damage rate vs. time history. This curve can be integrated to show a cumulative damage vs. time history. This curve can be used simply for visualization purposes, or to train probabilistic time series models (e.g., autoregressive models) to generate probabilistic damage estimates using the time series rather than sampling probability distributions.

Another option after extracting a cycle, is whether to subtract the cycle period from the remainder of the time series history. If the cycle period is not removed, the cycle time would be “double-counted” as occurring during both the extracted cycle and the half cycle it was extracted from. Enabling “time removal” would assign dwell time to only the extracted cycle, resulting in a shortened residual half cycle from which the extracted cycle was taken. This is illustrated below in Figure 6. A range formed by consecutive extrema interrupts an overall range. The middle plot shows the half cycle formed by the overall range after extraction in the case that time removal was not performed. The bottom plot shows the same in the event that time removal is enabled, resulting in a shorter (in the time dimension) residual half cycle.

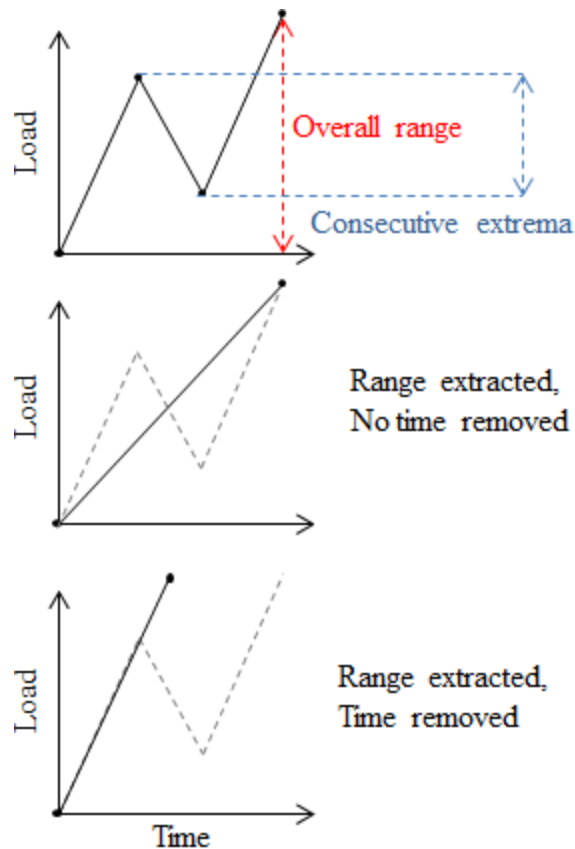


**Figure 6: Time removal illustration**

When this time removal is performed during fatigue analysis, it shortens the time-length of the residual half cycle form which two half cycles are extracted. In the event that significant time-dependent strains (e.g., creep strains) during the loading or the unloading of the test specimen, the cyclic stress-strain loop will look different if time removal is enabled or not. Assuming less time-dependent strain (in the case of enabled time removal) will make the loop smaller. In fatigue analysis, the fatigue damage is related to the area formed by the cyclic stress-strain loop. Therefore, enabling time removal will result in a lower damage prediction. Therefore, for fatigue analysis, time removal is not recommended since it will result in a less conservative damage prediction.

The overall process to perform the algorithm is shown below in the flowchart in Figure 7. First the time series data is imported. The series is rearranged to start at the most extreme value. In order to retain the cycle sequence of extracted half cycles, two time vectors are retained: one monotonically increasing “false time” vector starting at the minimum time value and one “true time” vector which keeps the original time stamp of the data point. If on-board memory is an issue, there could just be a function mapping the false time to the true vectors rather than saving both. This would be generated after the rearranging of the data to start at the most extreme point. When the time series is rearranged, the user can choose how much time is elapsed between the two parts to form one continuous history. The sampling increment can be used for this value, for example. Appending the two portions together assumes that the load history is periodically repeating and does not exhibit an upward or downward trend over time.

From this rearranged history, all the load reversals are flagged. This can be done in a logic mask, where every index (corresponding to the false time vector) at which a reversal occurs is marked with “true,” and all other points are marked as “false.” When a reversal falls on a flat peak (i.e., the load dwells on a constant value for consecutive time indices), the middle index should be selected as the reversal index.

Next, the reversals are evaluated by conventional three-point rainflow cycle extraction criteria [2], shown below in Figure 8. If a range is smaller or equal to a preceding range, it is removed from the history. If the algorithm is evaluating the first point in the history, one half cycle is extracted and all data until the next reversal is removed. If the first point in the history is not under consideration, the two reversals under consideration are removed and all points until the end of the second half cycle are

also removed (shown in Figure 10). If time removal is enabled, the elapsed time of the extracted ranges is removed from the remained of the history.

For the first half cycle, the elapsed time is calculated between the two extrema under consideration. Shown in Figure 9. If the second half cycle is also being extracted, the end time is interpolated to find the time when the load is again equivalent to the first reversal. If the end of the second half cycle falls on a flat region, the middle index should be selected. Next, for each half cycle, the user-input load range threshold,  $L$ , is used to calculate the upper and lower dwell time. The time corresponding to the upper value minus  $\text{range} * L$  and the time corresponding the lower value plus  $\text{range} * L$  is interpolated. These two times are used to section the total half cycle time between the upper dwell, ramp time, and lower dwell regions. For each extracted half cycle, the entry from the “true time” corresponding to the original start time of the half cycle is recorded. Therefore, a six-entry long row in the output matrix can be formed for each extracted half cycle: range, mean, first dwell time, ramp time, second dwell time, and start time.

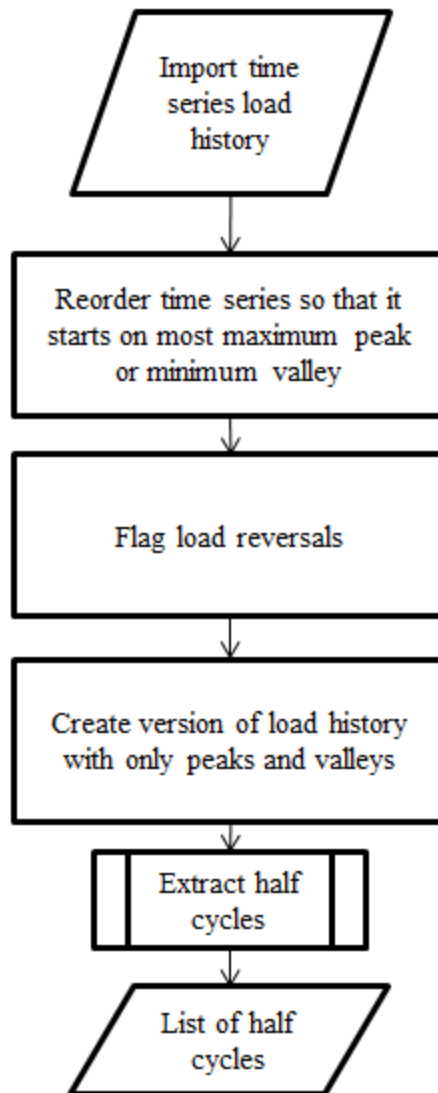


Figure 7: Flow chart for the proposed algorithm

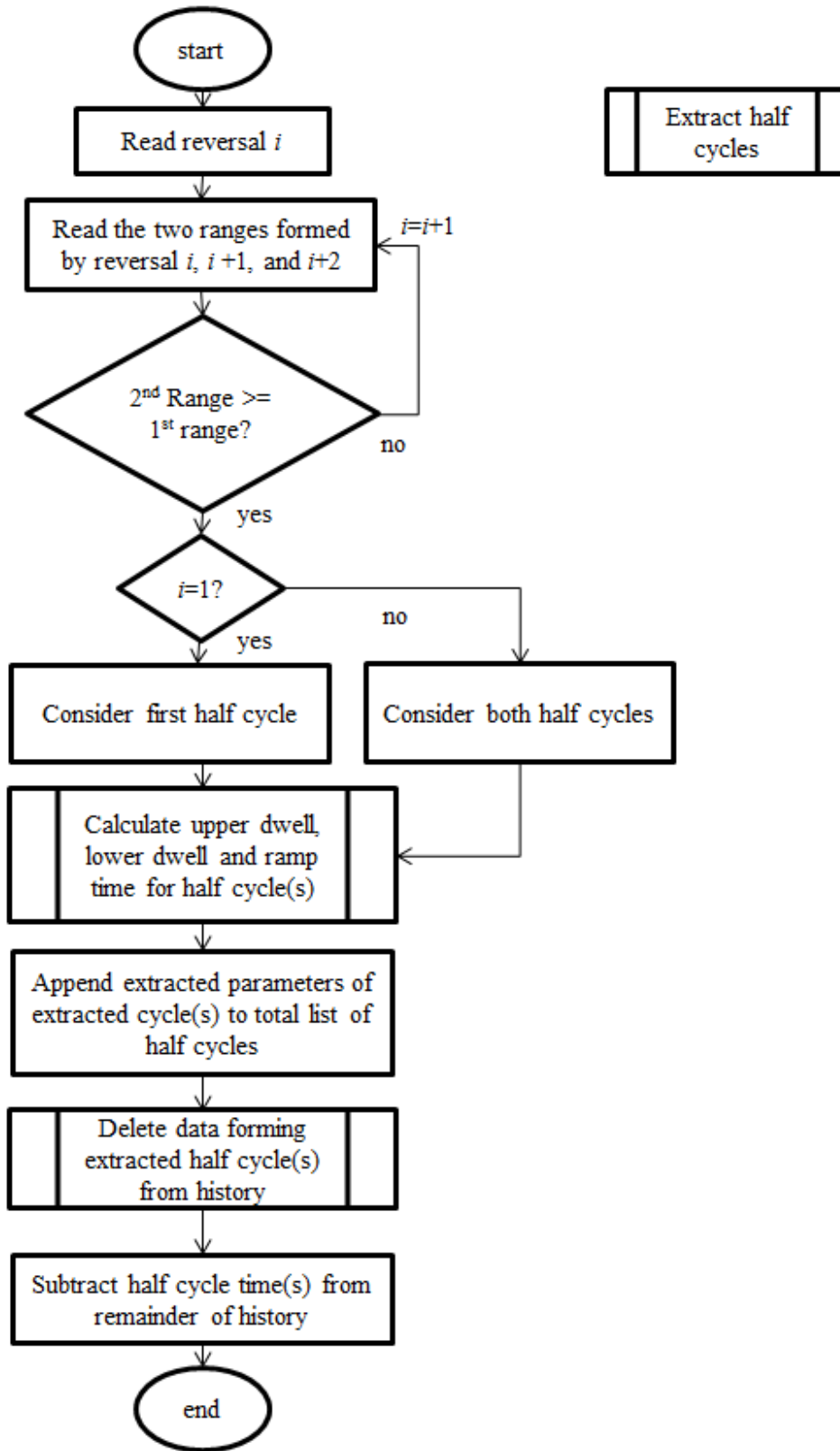


Figure 8: Detailed flowchart for the half cycle extraction step

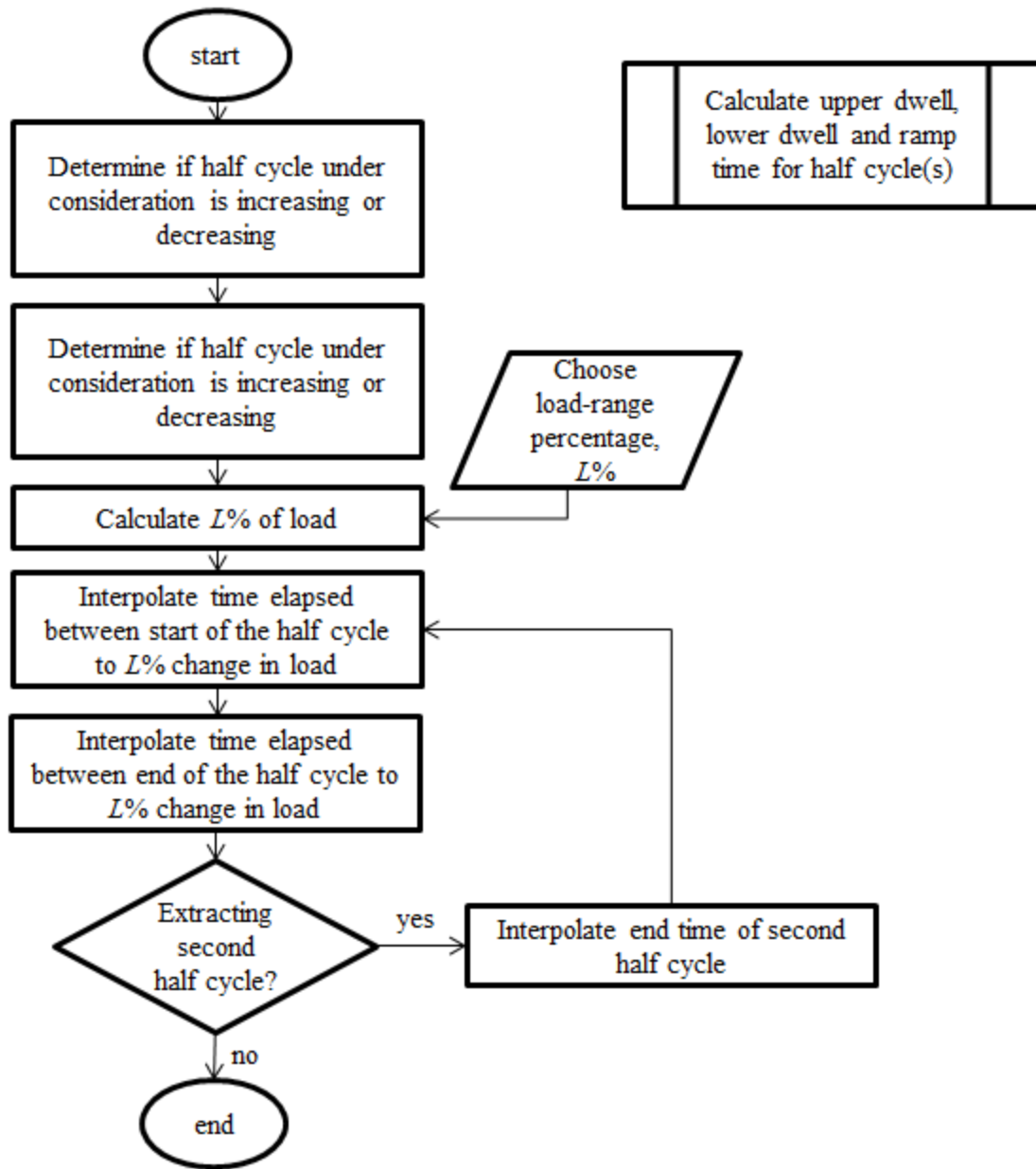
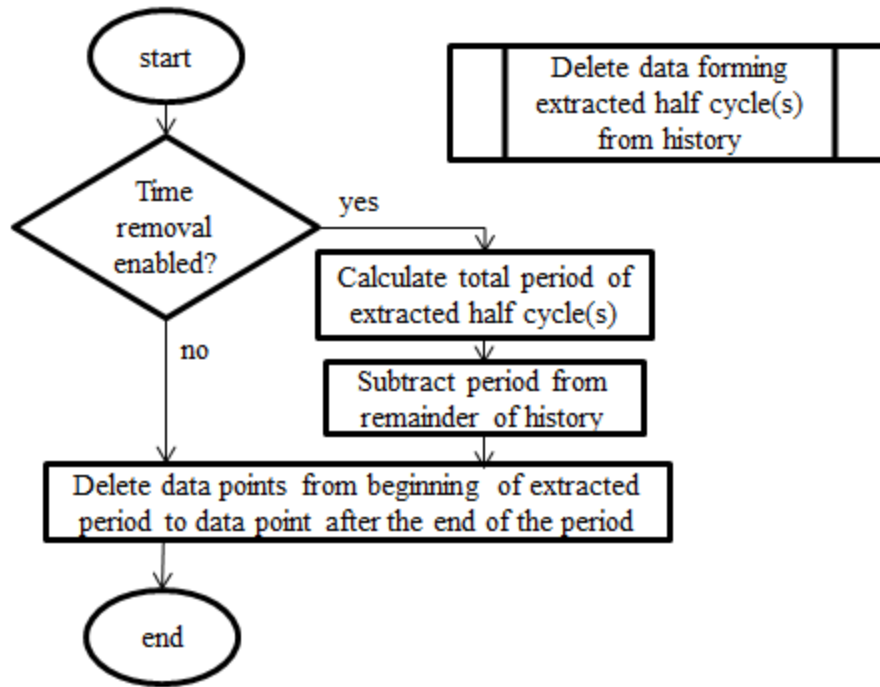


Figure 9: Detailed flowchart for the dwell time calculation step



**Figure 10: Detailed flowchart for the data deletion step**

In conventional two-parameter rainflow counting, the output results would be binned into a matrix. However, because of the additional extracted parameters, there is a disadvantage of binning. First, simply because of the larger number of parameters in itself, the bins will tend to be sparse (due to the “curse of dimensionality”), reducing the usefulness of binning at all. Balancing this fact against the possible discretization error in rounding cycles into bins, an engineer may choose to simply analyze the cycle list without binning. If binning is performed, a list of bins (with each bin corresponding to a unique combination of extracted parameter levels) will often be a more efficient storage structure than a full multidimensional histogram due to the likely sparsity of the array. If time removal is disabled, there may be extreme values of dwell time in long datasets that may substantially increase the bin width calculated by existing optimal bin width formulas, degrading damage predictions. In this case, non-linear bin spacing may prove

advantageous. In many cases, dwell times are observed to have a highly skewed distribution, with much more density towards the low end. However, because some higher values are observed, the bins will widen to accommodate the full range. This degrades the resolution of the histogram at the low end (where density is highest) and potentially causes inaccuracies. Future work to solve this problem may include optimal binwidth algorithms with non-linear spacing for highly skewed, long-tailed distributions (such as lognormal).

### **3.2 Comparison to prior methods**

For purposed of comparison, the new algorithm featuring a range-threshold based dwell definition was run on four different datasets, shown below in Figure 11. They were also processed using Cluff's [26] half-cycle time definition of dwell time, and Vichare's supplemental [29] algorithm for extracting dwell times.

The first dataset is a thermal cycling test profile used by Chai [36]. This profile is a periodically repeating temperature pattern recorded in a thermal cycling chamber. The temperature cycling history consisted of small cycles (having a mean of 65°C and amplitude of 20°C) superimposed onto the top peaks of larger cycles (having a mean of 25°C and an amplitude of 100°C). The large cycle represents a system being turned on for the day, and the minicycles represent variations in usage throughout the day. The temperature sampling period was one minute and the length of the history file is 8,486 minutes. After performing rainflow counting, the half cycle density (the observed half cycles divided by the total number of data points) is 0.11 half cycles per data point. There are 27 unique values of temperature observed over a range of 100°C. To quantify the amount of the history that is dwelling at a constant temperature, a "dwell fraction" is

calculated by counting the number of data points preceded by a point at the exact same load, then dividing by the total number of data points. The dwell fraction for this data set is 0.58. To quantify the amount of nonlinearity between extracted extrema, a “non-linearity parameter” is calculated by finding the maximum deviation between the load path and a linear path between the two extrema as a cycle is being extracted, normalized by the extracted range, summed for every extracted half cycle, and divided by the total number of half cycles. This parameter is about four times higher for the test dataset than the next (outdoor) dataset.

A second dataset was recorded from an outdoor telecommunications application. It is a temperature measurement from a circuit board, rather than the ambient temperature. This dataset tends to have less consecutive points occurring at the same load (“flat regions”) and features several high amplitude cycles where the temperature drops abruptly for several data points. There is a relatively small amount of monotonic data between reversals as a consequence of the large sampling period compared to the large swings in temperature. The temperature was sampled every fifteen minutes for 10,050 minutes. The half cycle density is 0.54 half cycles per data point. There are 657 unique values of temperature spread over a range of 45.6°C. The dwell fraction of this data set is 0.021. This dataset has the smallest non-linearity parameter out of all datasets considered.

A third dataset is from a laptop central processing unit temperature sensor. This data was sampled at one point per second for 36,668 seconds. This gives it a much higher sampling rate than the other three datasets. There are 0.47 half cycles per data point. There are 151 unique values of temperature spread over a range of 19.9°C. The dwell

fraction of this data set is 0.20. The non-linearity parameter in this data set is about twice as high as in the outdoor dataset.

A fourth dataset was recorded on a desktop graphics processing unit temperature sensor. The temperature was sampled every minute for 19,649 minutes. The observed half cycle density was 0.28. There were 12 unique temperature values over a range of 17°C. Of the four data sets, this one was the most discretized (e.g., smallest number of unique values). These datasets are illustrated below in Figure 11. These datasets will be referred to as “test profile”, “outdoor”, “laptop” and “desktop”, respectively. The dwell fraction of this data set is 0.70. This is the highest dwell fraction out of the four datasets, which is likely a consequence of the discretized temperature values. The non-linearity parameter is about four times as high as in the outdoor data set.

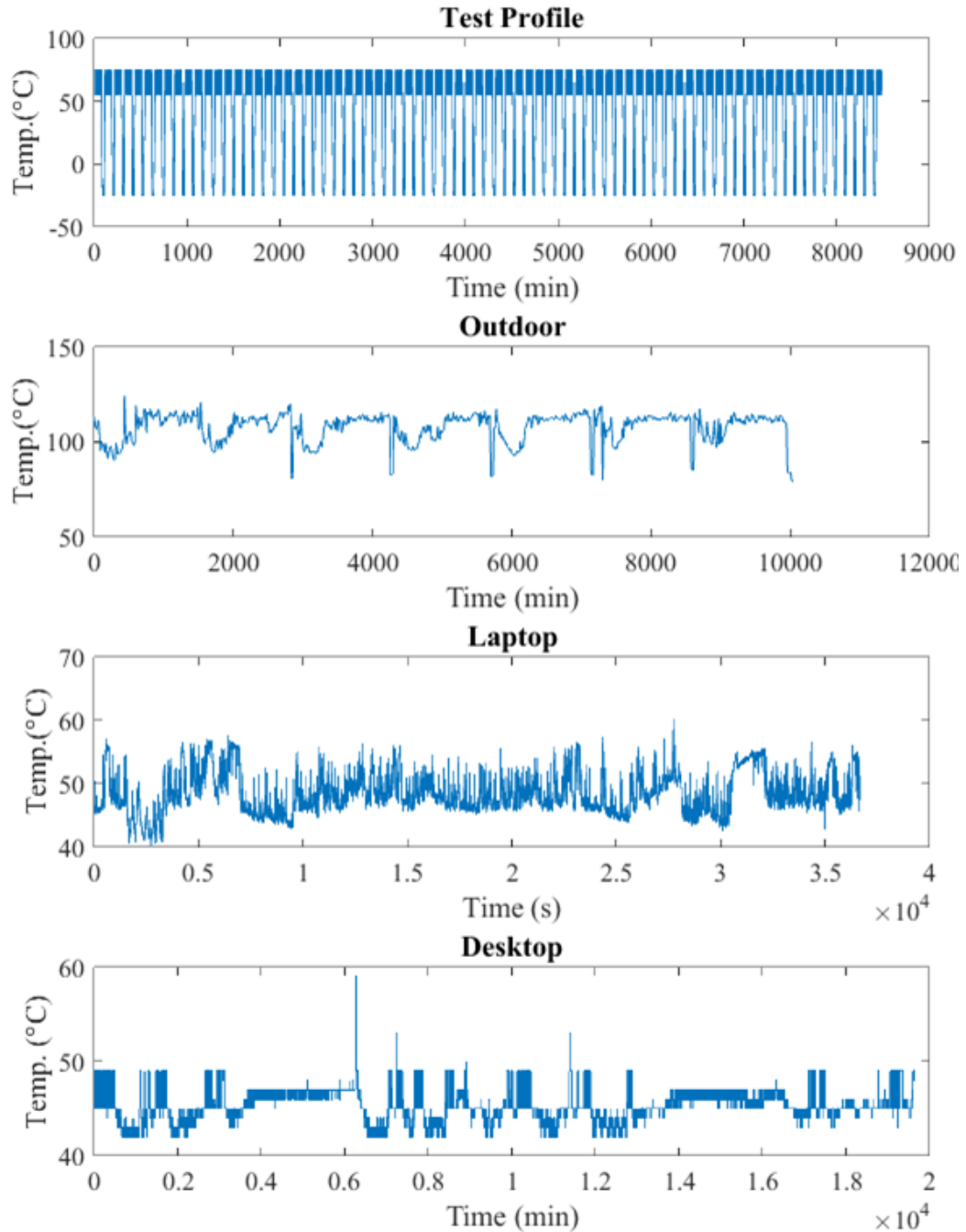


**Figure 11: Each of the four data sets under consideration**

The average dwells, without time removal enabled, are given below in Table 1.

The average dwells are somewhat correlated to the sampling rate, with the outdoor dataset consistently causing the highest average dwells. This could be a consequence of

less small (in range), short (in time) cycles being extracted which could only be picked up by a high sample rate, such as in the laptop dataset. For the proposed algorithm, a load-range percentage of 25% was used to define dwell. This was chosen because this would give the same result as a 50% half cycle time prediction (Cluff’s dwell definition) in the event that there was no monotonic data between two extrema, or if that monotonic data was purely linear.

**Table 1: Average dwell values**

|              | Cluff | Vichare | Proposed | Units |
|--------------|-------|---------|----------|-------|
| Test profile | 4.5   | 5.2     | 7.2      | min   |
| Outdoor      | 55.6  | 30      | 62.8     | min   |
| Laptop       | 5.2   | 1.3     | 7.8      | s     |
| Desktop      | 6.6   | 4.9     | 9.3      | min   |

The normalized average dwell estimations for the outdoor, laptop and desktop data sets are shown below in Figure 12. In the top figure, for the test profile data set, each estimate is normalized to the Vichare’s method estimate since it most literally finds flat regions in a data set where such flat regions occur. In the bottom figure, each bar is normalized to the prediction shown in the red bar. For the proposed algorithm, the load-

range percentage of 25% was again used. For Vichare’s method, the estimate was made with a 0°C/s rate threshold and a 0°C range threshold.

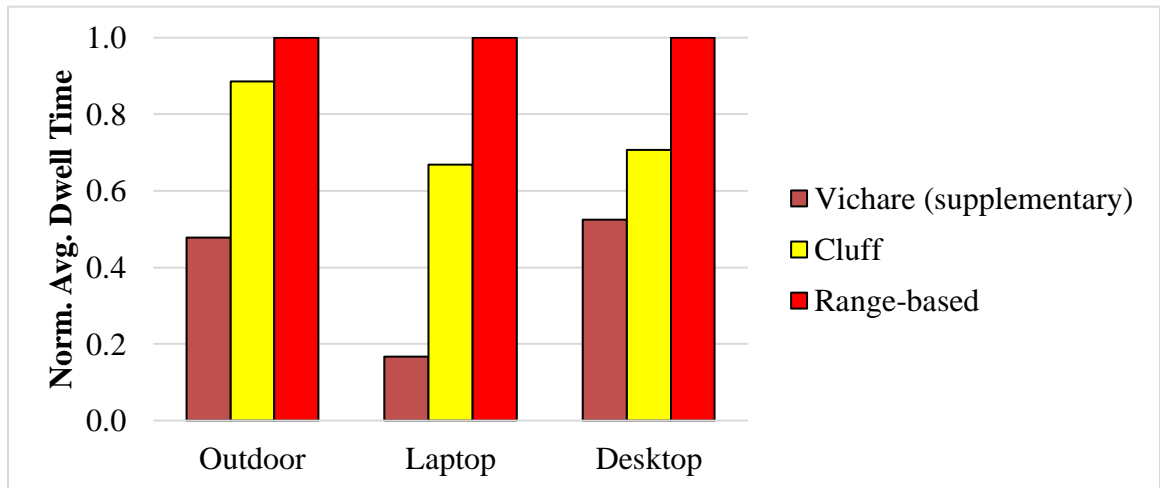
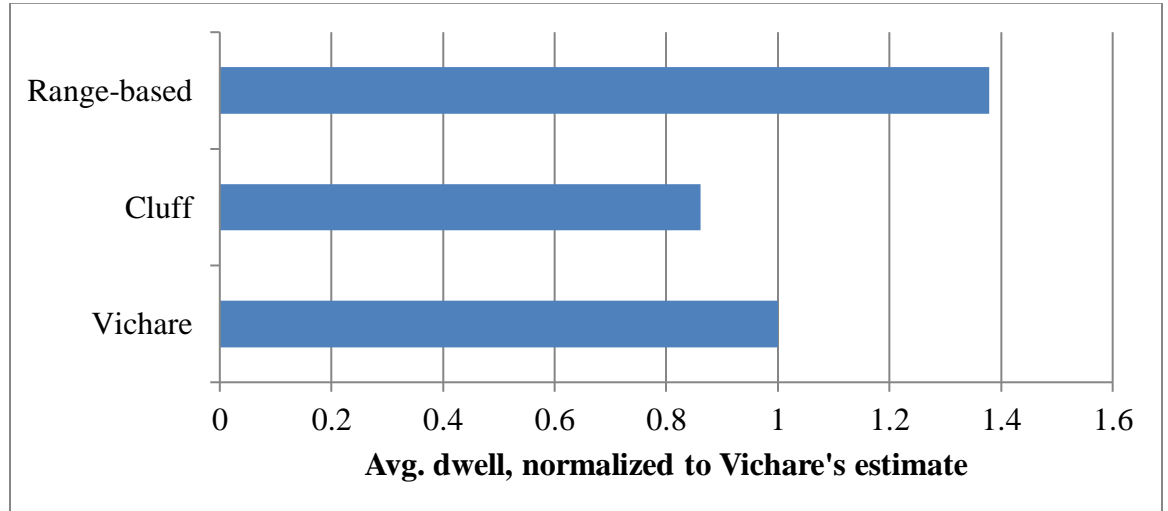


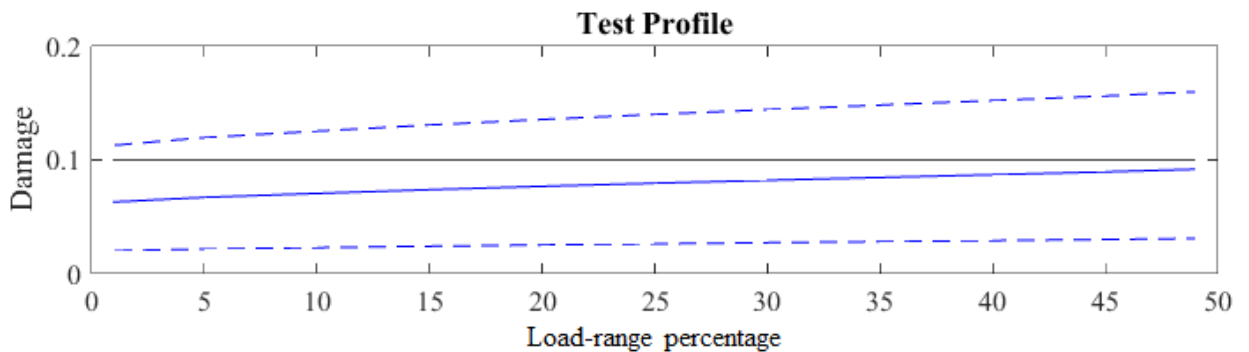
Figure 12: Average normalized dwell times for test profile (top) and the three remaining estimates (bottom)

The damage per half cycle was calculated with Engelmaier’s model using the material and geometry constants reported by Chai [30]. The total damage was summed linearly with Miner’s rule. Because the damage is calculated in the same way as Chai, the results can be compared to those experimental results. Below in Figure 13, the black line is the experimental results. The recorded history file was approximately ten percent of the

length of the reported time to 50% failure of the sample population. Therefore, the damage is shown on the graph below at approximately 0.1 to represent the fraction of life consumed at the end of the history file.

The blue lines are the damage estimate using Engelmaier's model, over a range of load-range percentages (the required input parameter to the proposed method). The solid blue line was calculated with an  $F$  value (the non-ideal factor in the Engelmaier model). This non-ideal factor is a function of package type. For this particular package type (leadless), the non-ideal factors are reported to be typically between 0.7 and 1.2 [10]. Therefore, the lower dashed blue line was calculated with an  $F$  value of 0.7 and the upper blue dashed line was calculated with an  $F$  value of 1.2. This gives some indication of the deviation between the experimental result and the estimate is within reason.

Although the estimate seems to improve at high values of load-range percentage, this single example cannot, by itself, be generalized to support the use of a high load-range percentage. Using 50% is classifying the entirety of each half cycle as dwell, while using 0% is not extracting any dwell time at all. This curve was calculated from 1% to 49%.



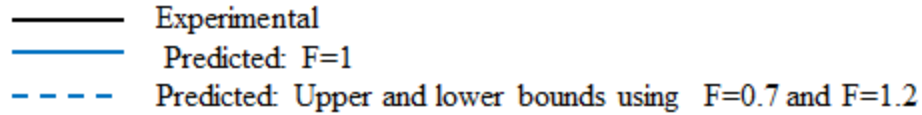


Figure 13: Comparison to experimental data

Next, Table 2 below shows the damage fractions at the end of each history for the rest of the data sets, using all three dwell definitions. The proposed definition- and the Cluff definition-based dwell estimations are performed both with and without time removal.

Table 2: Estimated Damage

|         | Vichare | Cluff      |         | Proposed   |         |
|---------|---------|------------|---------|------------|---------|
|         |         | No Removal | Removal | No Removal | Removal |
| Outdoor | 9.0E-03 | 6.6E-03    | 3.9E-03 | 6.8E-03    | 4.1E-03 |
| Laptop  | 4.9E-05 | 8.2E-05    | 8.5E-07 | 1.1E-04    | 9.4E-07 |
| Desktop | 1.4E-04 | 1.2E-04    | 2.4E-05 | 1.3E-04    | 2.4E-05 |

The next chart, Figure 14, shows the same information normalized to the proposed result (no time removal performed). Similarly to the results showing the average dwell times, the Cluff and the proposed methods match closest during the outdoor dataset since that data exhibits the least amount of monotonic data between extracted extrema. The Vichare method's results do not follow a clear trend relative to the other estimated, which is expected since it does not define dwell as being contained within a particular cycle, unlike the other two definitions.

Enabling time removal in the laptop dataset decreased the damage prediction, almost to zero. More than in the other datasets, the extracted cycles left such little dwell time left in the history for the larger remaining half cycles that they were extracted from

so that the time-removal enabled damage estimate was attenuated by orders of magnitude. While the impact is not quite as large in the other two datasets, it still makes a 40% difference in the outdoor dataset and an 80% difference in the desktop dataset. Enabling time removal makes the damage prediction much less conservative, in all of these cases.

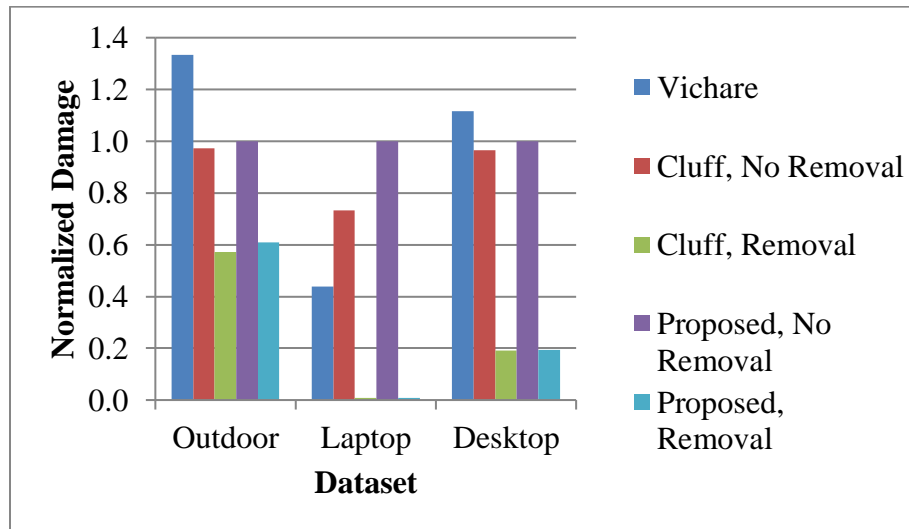


Figure 14: Normalized damage estimates

The percent differences between the damage results using the Cluff dwell time definition and the range-based (proposed) dwell time definition were within five percent both with and without time removal for the outdoor dataset. For the rest of the datasets, the predictions diverged. In Table 3 below, it can be seen that the difference in the test profile predictions, for example, are much higher (24% difference rather than 5%).

Table 3: Damage Comparisons between Cluff and proposed dwell definitions

|              | Damage |          | Diff. |
|--------------|--------|----------|-------|
|              | Cluff  | Proposed |       |
| Test Profile | 0.064  | 0.080    | 24%   |

|                           |        |        |    |
|---------------------------|--------|--------|----|
| Outdoor (time removal)    | 0.0039 | 0.0041 | 5% |
| Outdoor (no time removal) | 0.0066 | 0.0068 | 2% |

### 3.2.1 Comparison of Dwell Estimates

Since Cluff's definition of dwell time is a fixed damage fraction, it does not have a parameter to specify which impacts prediction. Vichare's supplemental algorithm and the proposed load-range based definition, however, each require input parameters. Vichare's algorithm allows small ranges and slopes to be treated as flat dwell regions. Therefore, the threshold for each ranges and ramp rates need to be specified in order to do this simplification. To analyze the sensitivity of the dwell predictions to the choice of input parameters, the average dwell time was estimated using range thresholds from 0°C to 10°C and ramp rate thresholds from 0°C/min to 2°C/min. For comparison, the average dwell estimate using the proposed load-range based dwell definition was also plotted on the right in Figures 15, 16, 18, and 20 below. The surface on the left graph is linearly interpolated within data points for the sake of visualization. The range threshold on the left graph (in °C) for Vichare's method and the range threshold (in %) on the right graph are different parameters. The former is the threshold below which all ranges are considered dwell, the latter is the threshold percentage of the cycle range near each extrema is defined as dwell within a particular cycle.

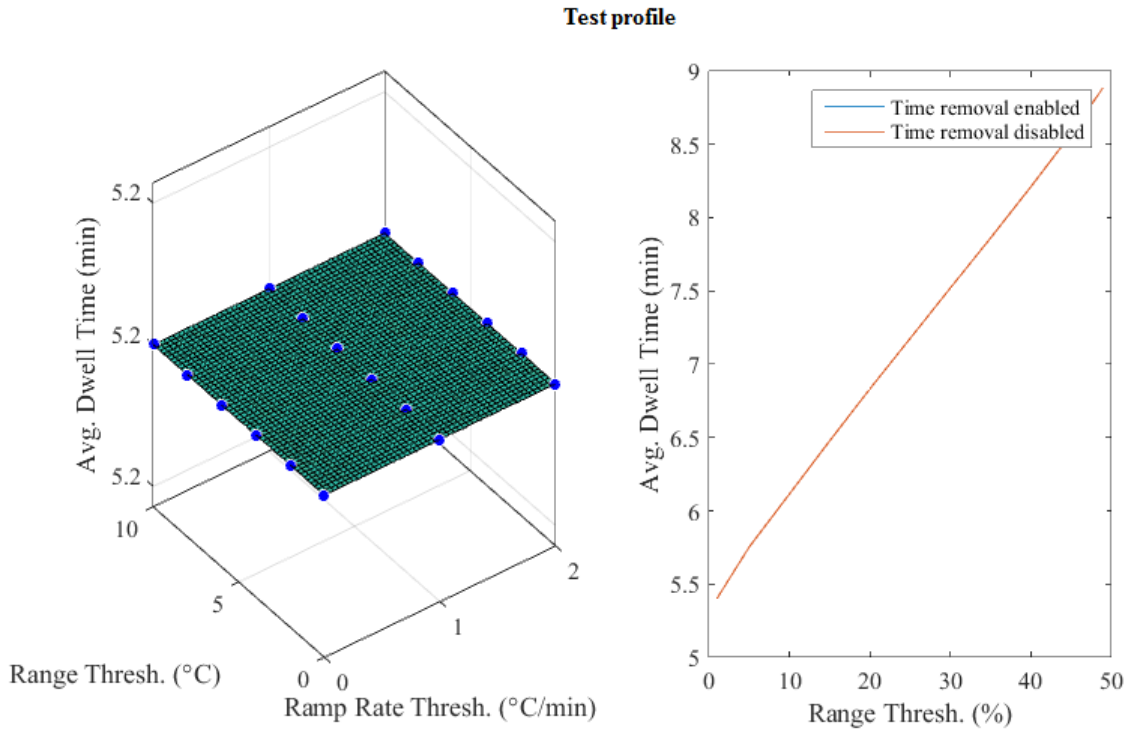


**Figure 15: Stability of average dwell time for proposed and Vichare methods for test profile data set**

For the test profile dataset, shown above in Figure 15, the average dwell times extracted by the supplementary algorithm are completely stable over the given range of both thresholds. This stable value, however, is lower than any of the average values extracted by the proposed load-range based algorithm. In this dataset, since all cycles are extracted on the first pass, there is no difference made by enabling time removal.

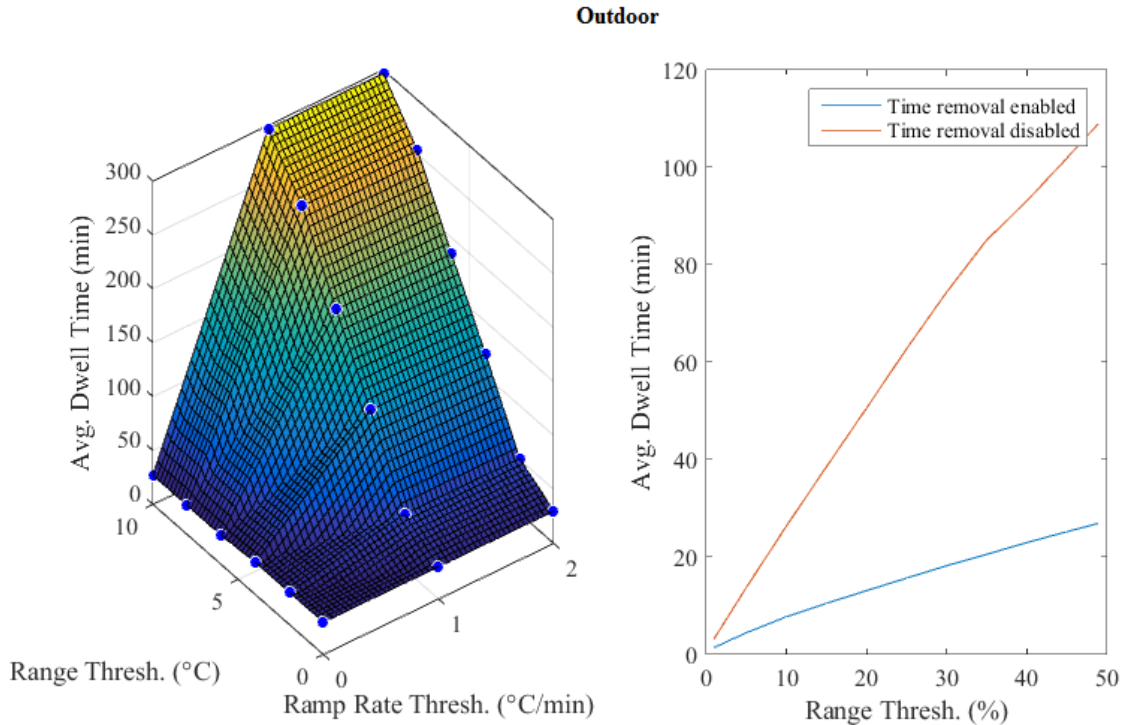


**Figure 16: Stability of average dwell time for proposed and Vichare methods for outdoor data set**

For the outdoor dataset, shown above in Figure 16, the supplementary algorithm gives a sharp rise in average dwell estimate at higher values of both ramp rate threshold and range threshold. Since this dataset features a very small amount of monotonic data due to the coarse sample rate relative to the rapidly changing load, there were few dwell regions extracted at all without increasing the threshold parameters. Setting both to zero, only seven dwells were detected. Increasing the ramp rate threshold to  $1^{\circ}\text{C}/\text{min}$ , the number of dwells detected peaked at a range threshold of two before dwells began to merge together at higher range thresholds, decreasing the number of dwells detected to 28 at a range threshold of  $10^{\circ}\text{C}$ . Increasing the ramp rate threshold to  $2^{\circ}\text{C}/\text{min}$  did not alter the results.

The average dwell predictions were also somewhat unstable for the proposed load-range based algorithm. The average increased as a function of range threshold percentage to almost 110 minutes, but only to about 25 minutes if time removal is enabled. Enabling time removal decreased the sensitivity to the average dwell estimates to the choice in range threshold percentage across all data sets analyzed (except the test profile, since every half cycle was extracted on the first pass so time removal had no impact).

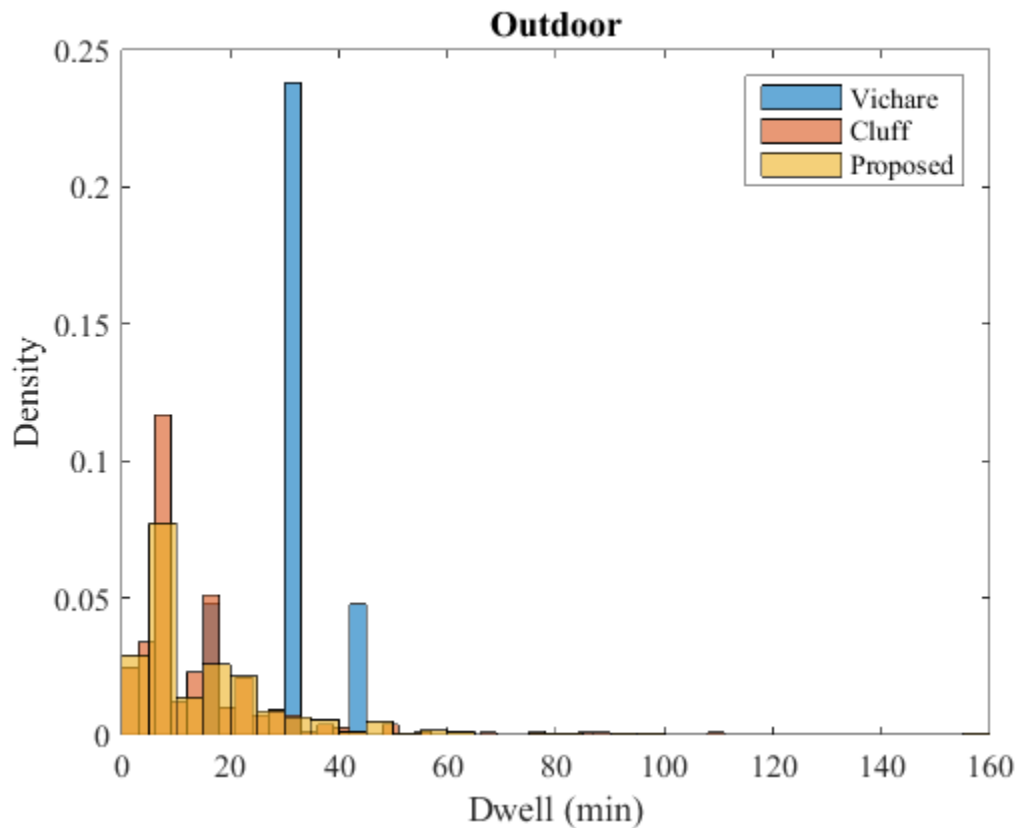
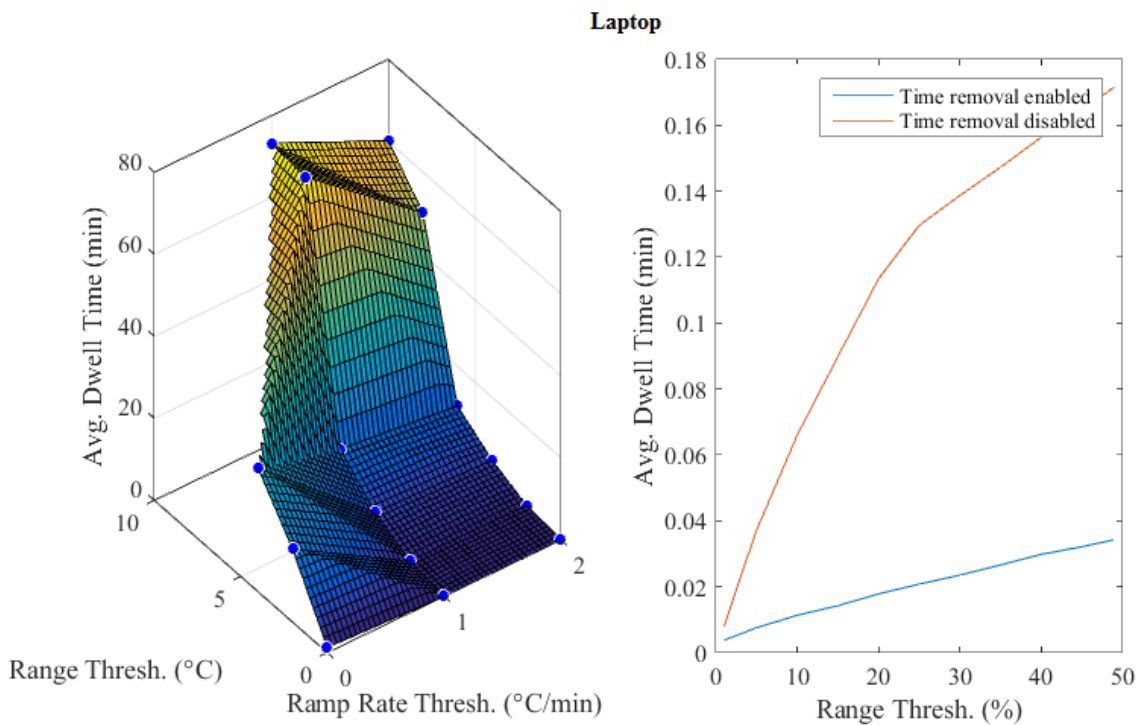


Figure 17: Distribution of dwell times for outdoor data set

Looking at the distributions rather than the averages (via a histogram), it is apparent that while the half-cycle time based definition (Cluff) and the load-range based definition (proposed algorithm) showed similar-looking distributions, the supplementary

algorithm (Vichare) showed a very different pattern. In this case, only a few dwells were detected in the history using the supplementary algorithm, giving a more discretized probability distribution compared to the other two. The distributions above in Figure 17 (and Figures 19 and 21 as well) were estimated using 25% load-range percentage for the proposed algorithm, and 0°C and 0°C/min for the supplementary algorithm. No time removal was performed. The optimal bin widths were determined using the F-D rule [19].



**Figure 18: Stability of average dwell time for proposed and Vichare methods for laptop data set**

In the laptop data set shown in Figure 18, the estimated average dwell time surged as a function of range threshold in the supplementary algorithm. At a range threshold of 0°C, there are 5629 dwell times extracted, but this number decreases to less than 50 across all ramp rate thresholds at a range threshold of 8°C and above. Because this data set does not have a lot of extreme values (relative to the outdoor set which experiences

large maximum ranges), setting the ramp rate threshold so high will classify most of the history as dwell periods.

For the proposed load-range based algorithm, the average dwell predictions varied from about 0.01 minutes to about 0.17 minutes. The range of values was again much smaller when time removal was enabled, making the high end of the range only about 0.035 minutes.

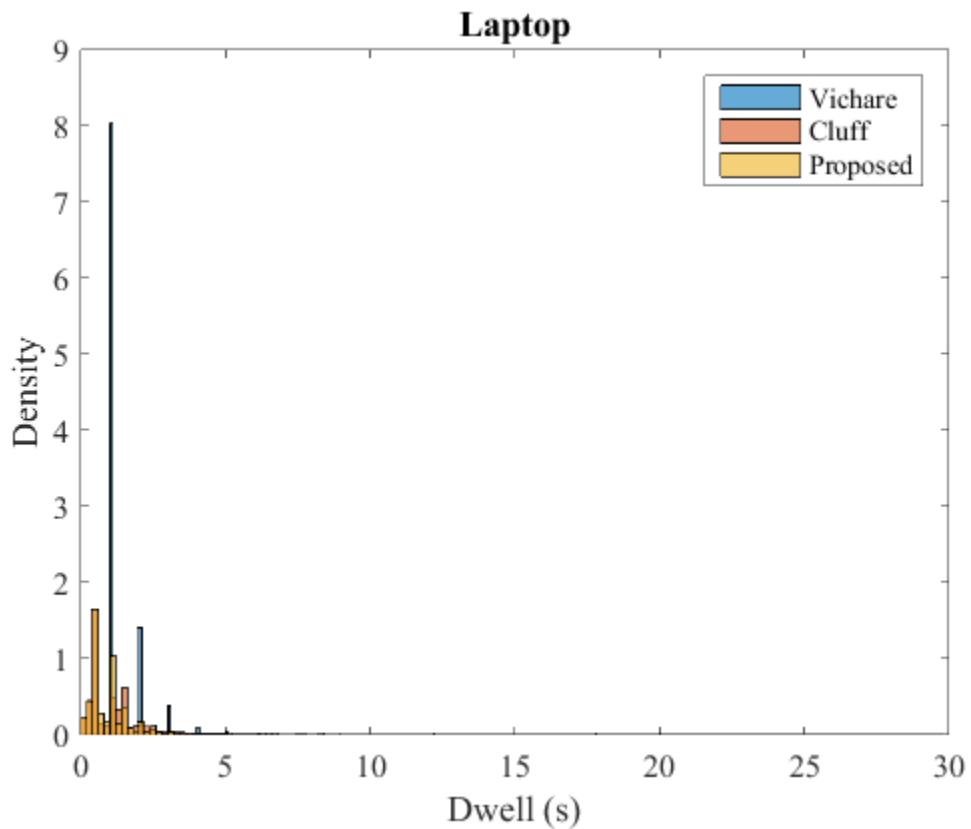


**Figure 19: Distribution of dwell times for laptop data set**

The distributions of dwells (in Figure 19 above) in the laptop dataset again looked similar for the time-based estimate and load-range based estimates, but varied most from the supplementary algorithm. All three distributions are skewed, so that higher densities are observed towards the lower dwell times.

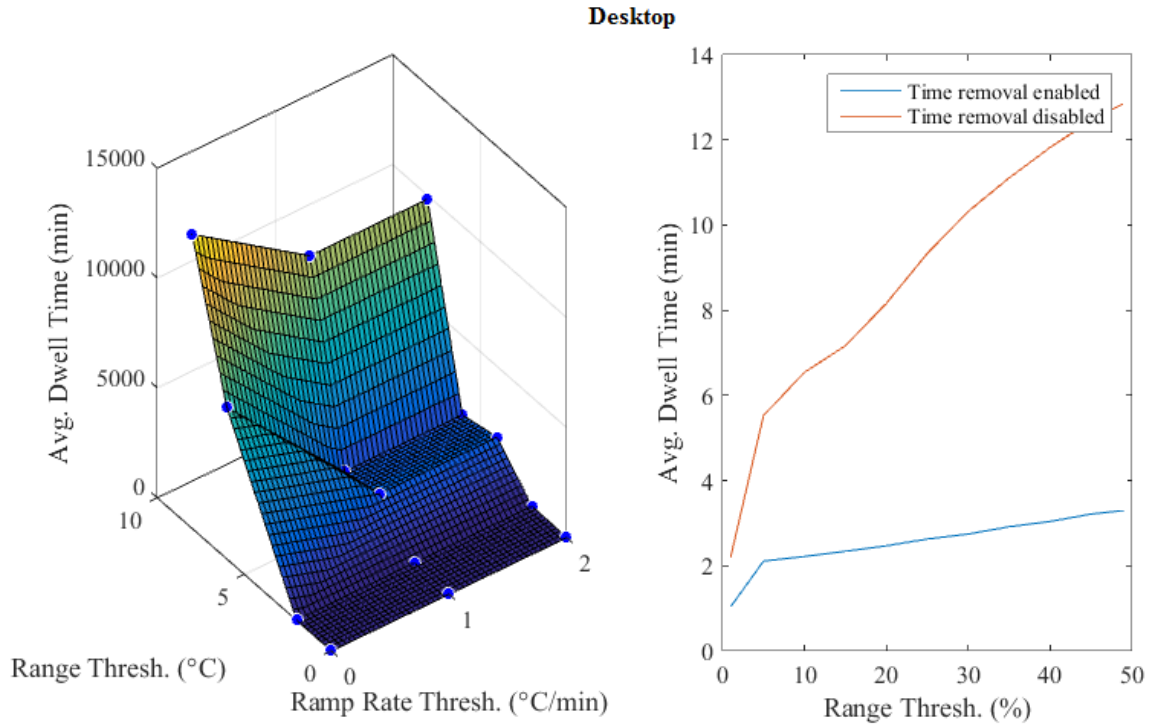


**Figure 20: Stability of average dwell time for proposed and Vichare methods for desktop data set**

In the desktop dataset, the range of values that the temperature took was fairly small compared to the range thresholds (for the supplementary algorithm) analyzed in Figure 20. At the higher end of range thresholds in the supplementary algorithm, almost the entire history is characterized as a dwell time, leading to average dwell predictions of over 10,000 minutes. In the proposed load-range based algorithm, the estimated dwells showed a similar pattern as the outdoor and laptop datasets, where the time removal decreased the apparent sensitivity of the estimates on range threshold percentage.

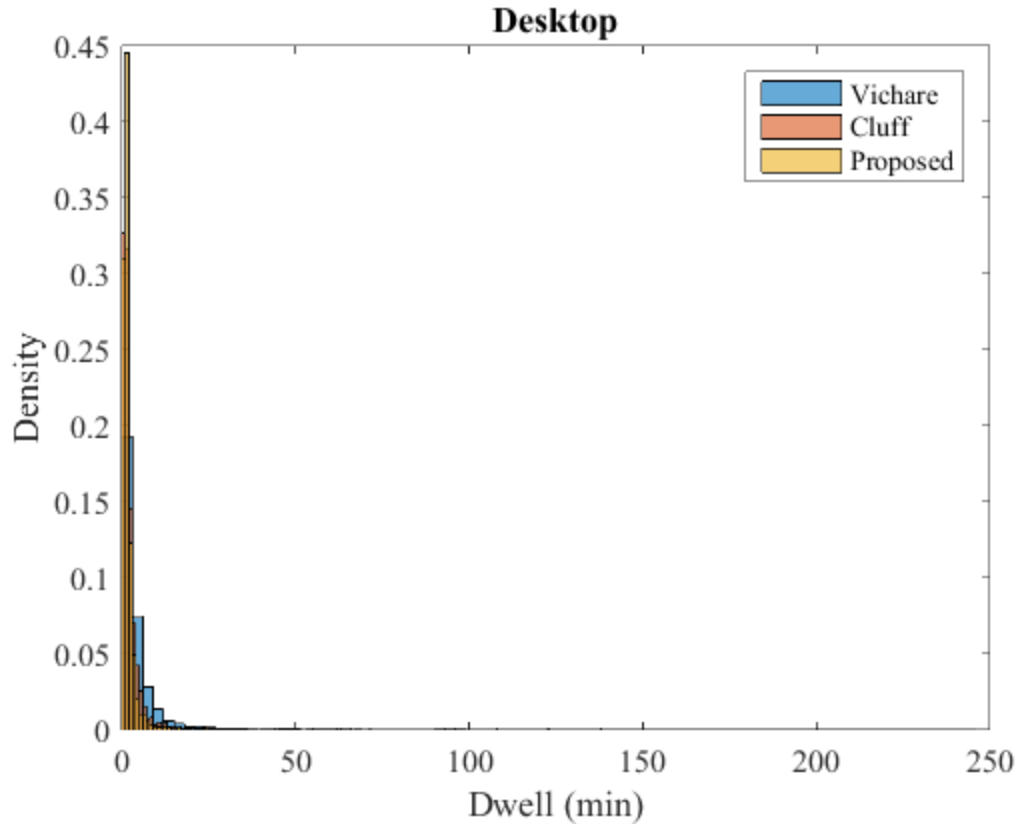


**Figure 21: Distributions of dwell estimates for desktop data set**

The distributions (shown in Figure 21) for all three methods look visually similar, with the supplementary algorithm having a slightly higher density at higher values of dwell time, and the time-based and load-range based estimates conversely having higher densities at lower values.

### 3.2.1 Comparison of Damage Estimates

For each of the data sets, all of the following damage predictions using Engelmaier’s model (using material and geometry constants from [25]), and Miner’s rule. For the damage estimates using Vichare’s method (using a supplemental algorithm for extracting dwell time with  $0^{\circ}\text{C}$  as the range threshold and  $0^{\circ}\text{C}/\text{min}$  as the ramp rate threshold), probabilistic predictions were generated using a Monte Carlo simulation with

distributional correlations modelled with Gaussian copulas. For the estimates using the time-based definition of dwell (Cluff) and the load-range based definition of dwell (proposed algorithm), deterministic predictions were made using Engelmaier's model (with the same constants as before) and Miner's rule in the same way. The load-range percentage for the proposed algorithm was set to 25% to match the Cluff method most closely.

In the outdoor dataset, estimates using Vichare's algorithm tended to be more conservative since, on average, higher dwell times were used than in with the other two methods (shown below in Figure 22). The predictions of the Cluff and proposed methods matched fairly closely to each other. This is expected, since with the relative lack of monotonic data in this dataset, the two methods estimated dwell times the same if there is no monotonic data between extrema. Enabling time removal reduced the damage estimates by almost 50%. The estimates without time removal fell within the uncertainty bounds estimated by the Vichare method, but enabling time removal moved the estimates to the lower extreme.

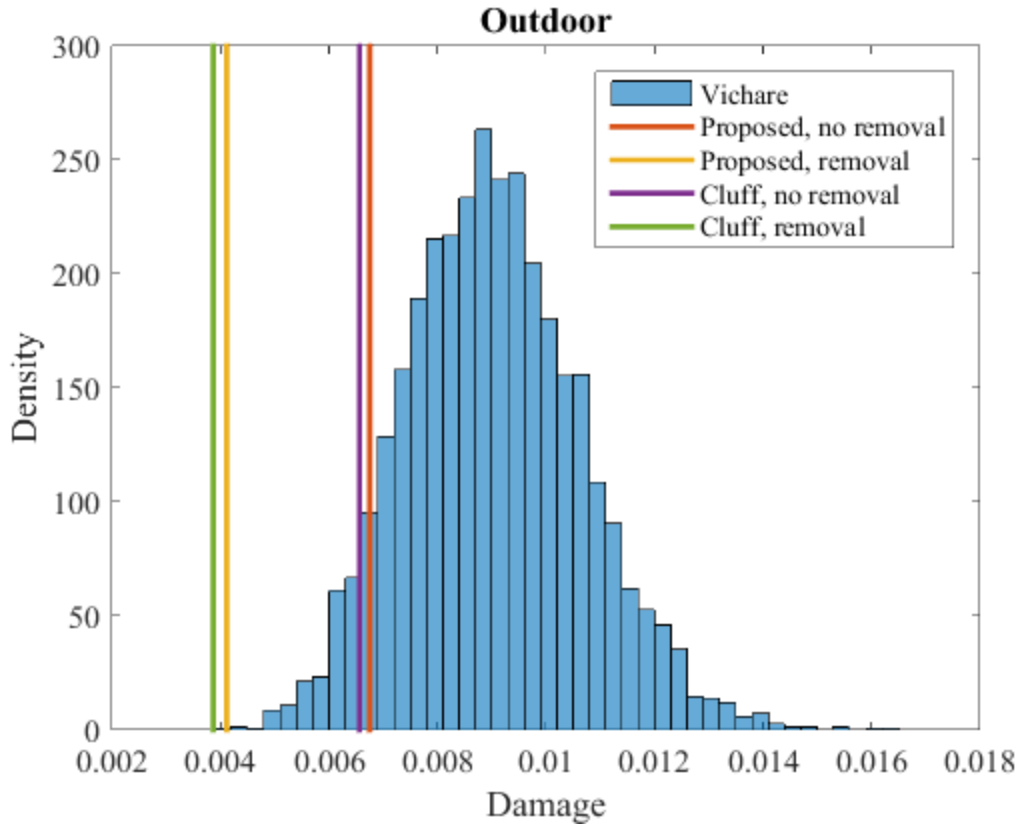


**Figure 22: Damage comparisons for outdoor data set**

In the laptop dataset, none of the estimates well within the distribution estimated by the Vichare method (as shown below in Figure 23). The proposed method without time removal ended up being the most conservative estimate (highest damage prediction), followed by the Cluff estimate without time removal, and then followed by the Vichare estimate. Enabling time removal reduced the damage estimates by an order of magnitude, due to the small cycles being extracted from larger cycles “using up” all of the dwell time, reducing the impact of the larger ranges.

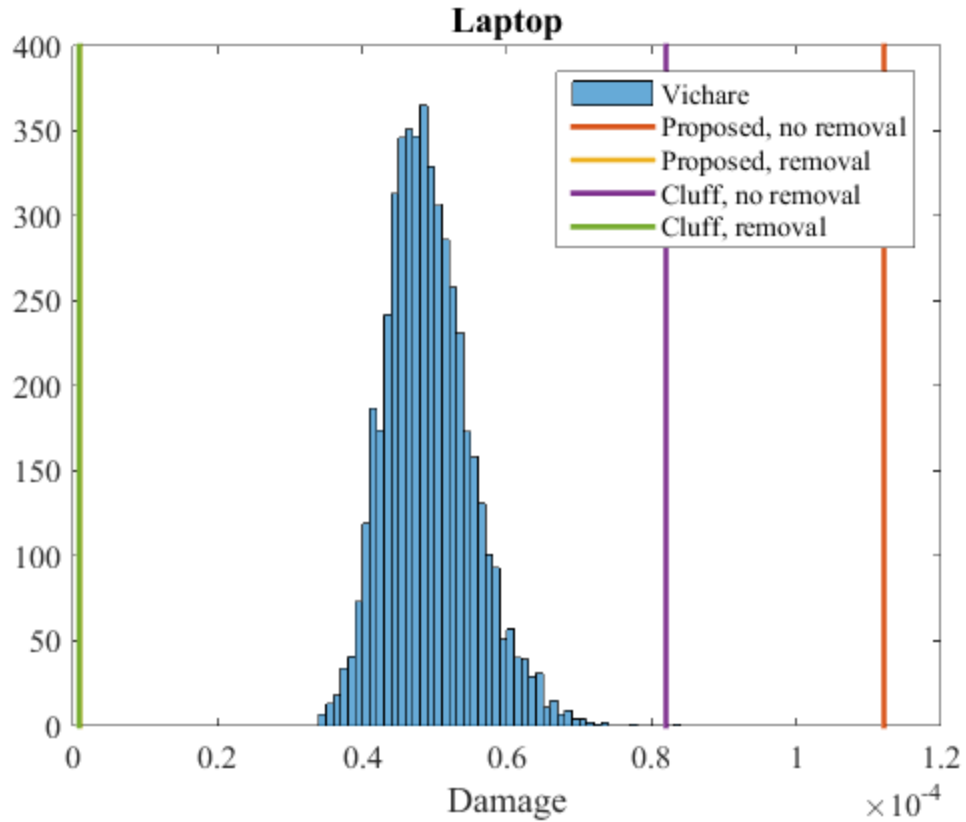


Figure 23: Damage estimates for laptop data set

In the desktop dataset, the proposed method and Cluff method’s deterministic predictions fell within the distribution estimated by the Vichare method (shown below in Figure 24). More of the mass of the distribution, however, is higher than either of the estimates, making Vichare’s method the most conservative in this case.

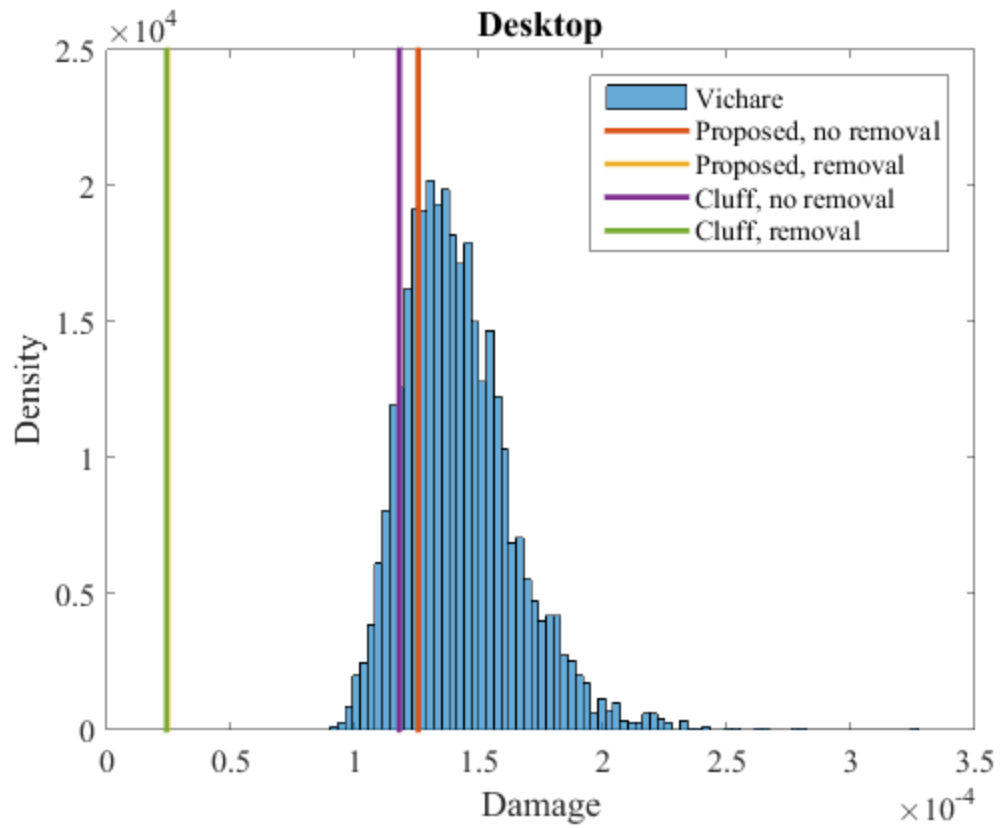


Figure 24: Damage estimates for desktop data set

### 3.3 Stability of Damage Estimates in the Proposed Algorithm

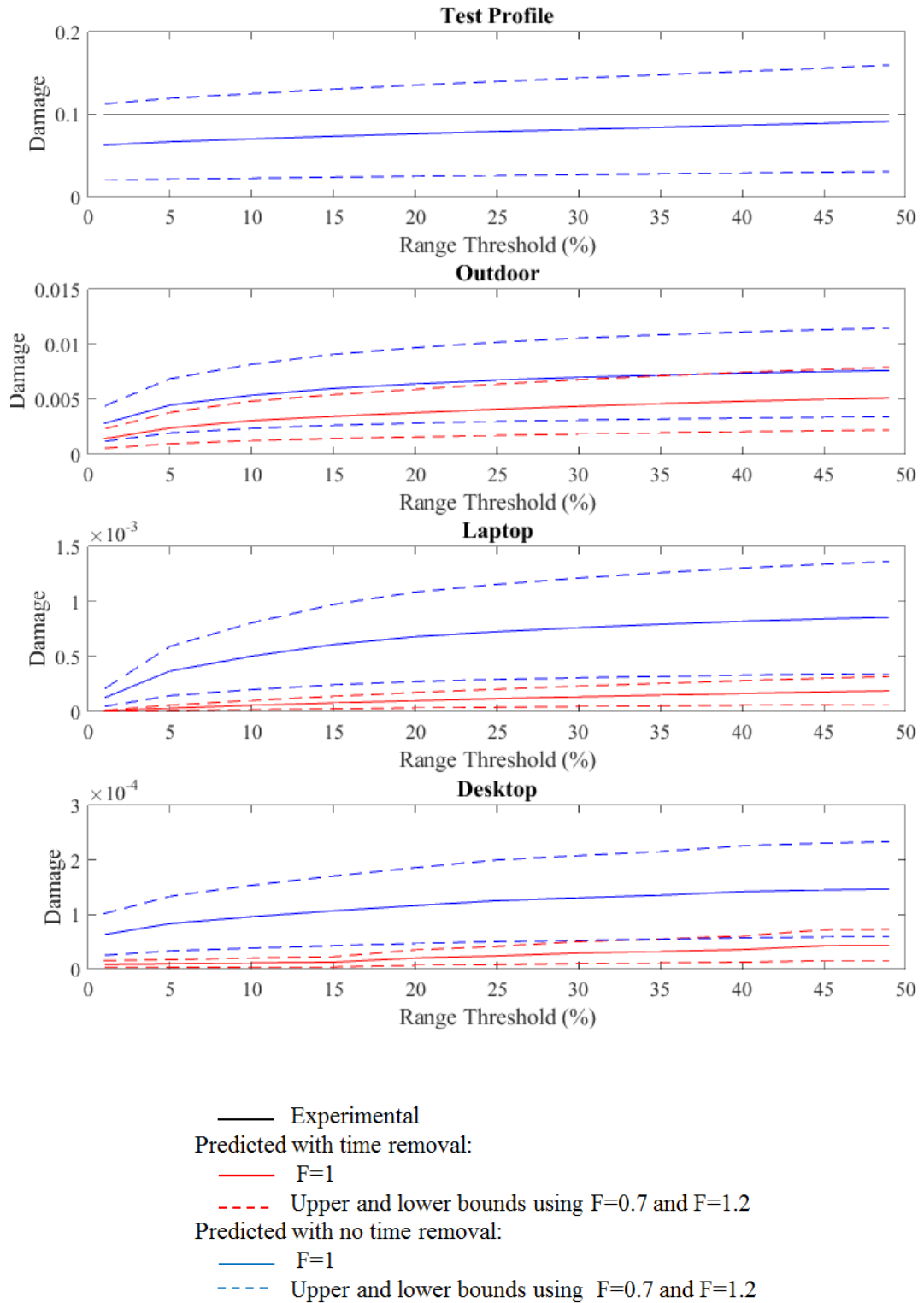


Figure 25: Stability of damage estimates for each data set

The damage estimates in all cases varied strongly as a function of range threshold percentage. In the plots above in Figure 25, the top graph is the same curve as shown in Figure 13 above. This shows the variation in damage estimate for the test profile dataset using the proposed load-range based dwell definition and a load-range threshold percentage of 25% with Miner’s rule and Engelmaier’s model using a non-ideal factor of 0.7 (lower dashed blue line), 1 (solid blue line), and 1.2 (upper dashed blue line). However, in this dataset, it made no difference whether time removal. The results at load-range percentage of 25% are given below in Table 4.

**Table 4: Damage estimates**

|              | Predicted damage, time removal |         |         | Predicted damage, no time removal |         |         |
|--------------|--------------------------------|---------|---------|-----------------------------------|---------|---------|
|              | $F=0.7$                        | $F=1$   | $F=1.2$ | $F=0.7$                           | $F=1$   | $F=1.2$ |
| Test Profile | 0.021                          | 0.064   | 0.12    | 0.021                             | 0.064   | 0.12    |
| Outdoor      | 0.0016                         | 0.0039  | 0.0060  | 0.0029                            | 0.0066  | 0.0099  |
| Laptop       | 3.6E-05                        | 1.1E-04 | 1.8E-04 | 2.7E-04                           | 6.6E-04 | 1.1E-03 |
| Desktop      | 8.4E-06                        | 2.4E-05 | 4.1E-05 | 4.8E-05                           | 1.2E-04 | 1.9E-04 |

### 3.4 Stability over sampling rates

A primary driver in the data size of the history is the sensor sampling rate. A high sampling rate will fill up storage memory more quickly, and the resulting history will take more time to transmit (e.g., if a remote sensor needs to transmit wirelessly to a computer) and process. However, if the sampling rate is too low, details of the history could be missed. The sampling rate should be high enough to capture the fastest changing signal in the history.

The damage for the laptop dataset and desktop dataset was estimated using the same method as before (using a load-range percentage of 25% and a non-ideal factor of

1). Then, the damage was recalculated using every other data point. Then it was recalculated using every 3<sup>rd</sup> data point, and then every  $N$ th data point. The horizontal axis on Figure 26 below shows the  $N$  value, so at a value of one, every point in the original time-temperature history was retained. At a value of 60, every 60<sup>th</sup> point was retained in the original history to do the damage calculation. No noise filtering was performed on the original data.

For both histories, there was a general downward trend when time removal was not enabled. The desktop dataset decayed faster, but the original sample rate of the laptop dataset was 60 times faster (once per second rather than once for minute). However, when time removal was enabled, the damage estimates were stable (as a function of  $N$ ) relative to the no time removal estimates. However, as expected, the no removal estimates were consistently higher. This difference decreased as a function of  $N$ .

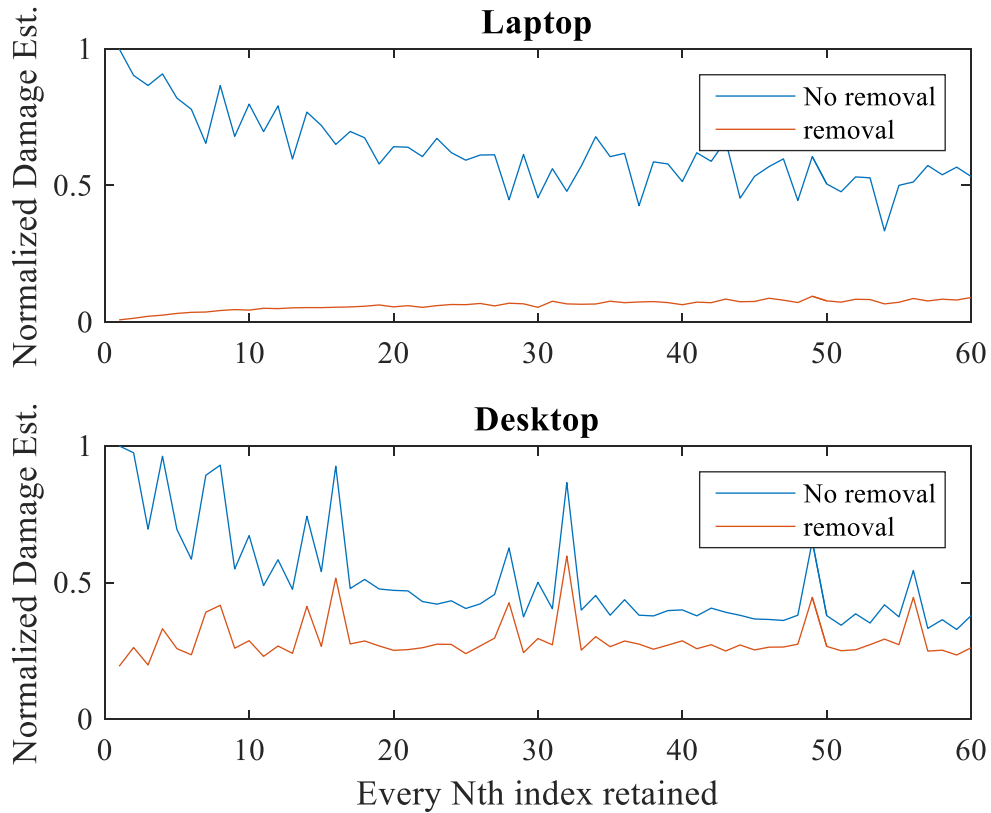


Figure 26: Stability of damage estimate over decreasing sampling rates

### 3.5 Stability over history length

When a long time history is segmented, it breaks up long cycles which would otherwise span the boundary between segments. This could heavily impact the large residual cycles left after rainflow counting, which in some case may span almost the entire original length of this history. However, if time removal is enabled, the residual cycles will be shorter (in the time dimension) and therefore a smaller sensitivity to history length is expected.

To explore this, a long time-temperature history was divided into  $N$  slices, and the damage was calculated for each segment. The damage was calculated using the same

method as before, with a long-range percentage of 25% and a non-ideal factor of 1. The damage for all segments in an iteration were summed for comparison's sake. The plot of normalized summed damage estimate (relative to the “no removal” unsegmented estimate) vs. number of segments is shown below in Figure 27. The damage estimate of the “no removal” version decreased about 20% after 70 segmentations.

While the stability over a range of segments does improve (i.e., the magnitude of the average rate of change is smaller), the damage estimate still changes. Relative to the “no removal” unsegmented estimate, the damage estimate increases about 7% after 70 segmentations. Relative to itself (the “removal” unsegmented estimate), the damage estimate increases about 35%. This analysis implies that, for a stationary load in this application, a damage estimate based on a small portion of the history will under estimate damage relative to an estimate on the full history if time removal is not enabled. Conversely, a small segment may overestimate damage of the full history if time removal is enabled.

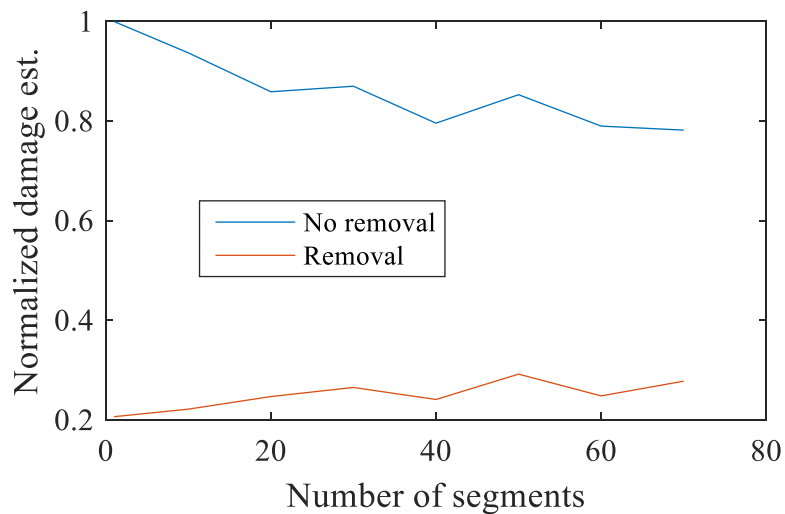


Figure 27: Stability of damage estimates over smaller history lengths

### 3.6 Comparison of Run times and Memory Requirements

Because the new method to estimate dwell time takes into account more details from the load paths between load reversals, it takes longer to run over a particular history. The biggest drivers in run time is the number of interpolations required by each. If neither the end of the second half cycle corresponding to a particular extracted range is not interpolated, nor the dwells, then the algorithm executes the quickest (out of the options considered). If the algorithm interpolates the end time of the second half cycle, but does not interpolate the dwells based on a load range definition of dwell time, the algorithm slows. It slows further if both the end of the second half cycle and both dwell period for each half cycle are interpolated.

As shown below in Figure 28, the run times scale approximately linearly with input history length, although they scale at different rates. Compared to the dwell interpolation, only performing the period interpolation results in about a 60% reduction in run time, while interpolating neither results in about a 90% reduction. As shown in Figure 29, there is a slight reduction in memory requirements if the monotonic data is not considered during extraction. If monotonic data was never saved in the first place, rather than being deleted by the algorithm itself, the difference between the two lines would be larger.

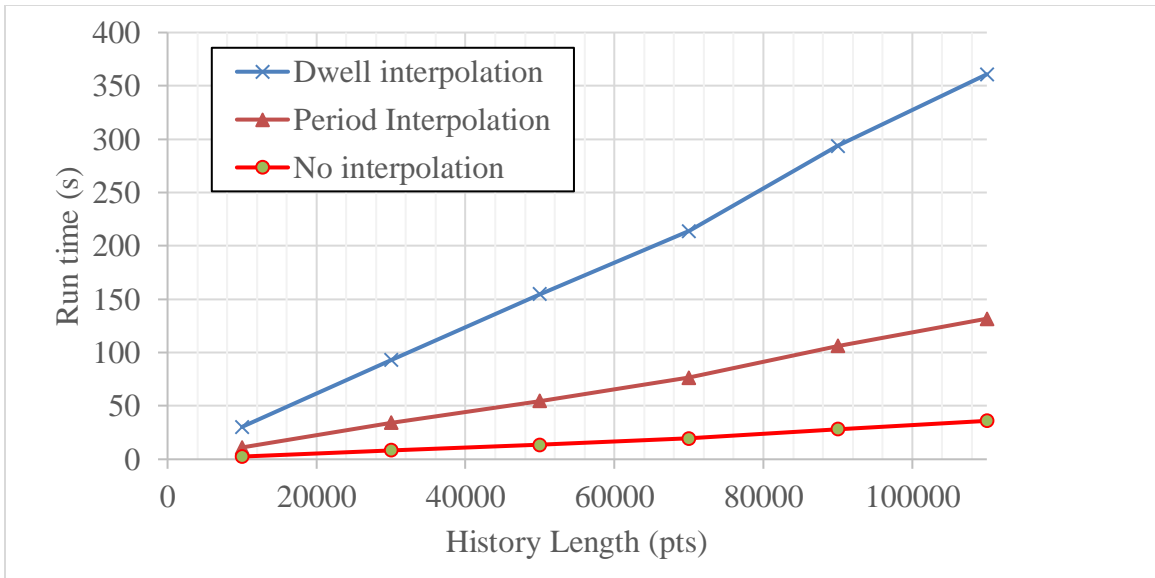


Figure 28: Run time comparisons

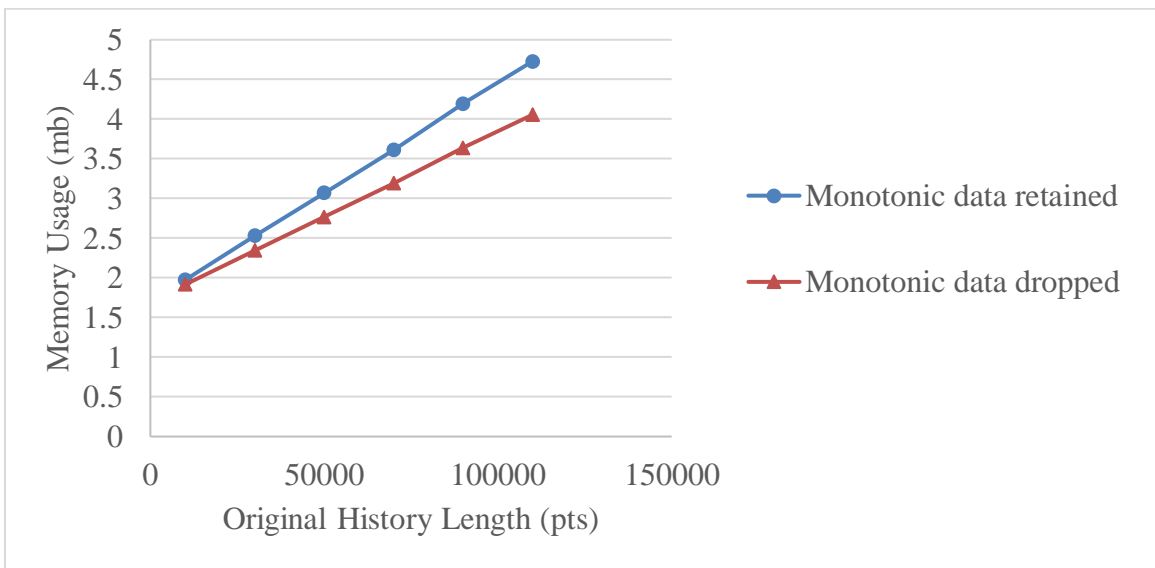


Figure 29: Memory usage comparisons

## Chapter 4: Automated Cycle Reduction

When using a damage estimate-based cycle reduction, it is necessary for the user to choose an acceptable level of damage reduction. An alternative is to use a statistical test to see if the distribution of observed damage rates during the history has changed

before and after reduction, within a particular confidence limit (e.g., 95%). The null hypothesis would be that the pre-reduction and post-reduction damage rate histories were from the same distribution.

#### **4.1 Proposed Algorithm**

The first step in this process is to calculate the distribution of damage rates. This can be done by converting the cycle list resulting from rainflow counting, along with the calculated damage per cycle, into a damage rate vs. time history. This requires that the half cycle time length and half cycle start time were extracted parameters during cycle counting. The damage for each half cycle is superposed equally onto the time indices from the beginning of the half cycle to the end. After superposing all half cycles onto the history, the damage contained in a particular time index is the damage rate (in units of time step of the history). If desired, the area under the curve corresponds to the total damage estimate. The vector of damage rates can be treated as a sample population of a random variable.

This baseline distribution can be used as a baseline iteratively compare distributions formed from removing low-damage cycles. After saving the baseline distribution, the cycle list is sorted in order of increasing damage per cycle. The damage rate vs. time history is recalculated with the least damaging cycle removed, and the distribution of damage rates is estimated in the same manner as the baseline distribution. The two distributions are compared with a statistical test to evaluate the null hypothesis that the two populations are formed from the same underlying distribution. Since the two populations are not independent, bootstrapping may improve (i.e., reduce bias of) the comparison by the statistical test.

For the following implementations, the two-sample Kolmogorov-Smirnov test was used to compare the distributions. This test calculates Kolmogorov-Smirnov statistic, which is the maximum distance between two empirical distribution functions. As the number of data points approach infinity, the Kolmogorov-Smirnov statistic will converge to zero if the two test functions are generated from the same underlying distribution. The null hypothesis is rejected at a level  $\alpha$  between a first sample size  $n_1$  and a second sample size  $n_2$  when the Kolmogorov-Smirnov statistic  $D_\alpha$  is greater than a critical value, or by comparing the asymptotic  $p$ -value to  $\alpha$ . This critical value can be found in a look-up table, or approximated by a formula assuming large sample sizes:

$$D_\alpha > c(\alpha) \sqrt{\frac{n_1+n_2}{n_1 n_2}} \quad (4.11)$$

$c(\alpha)$  is a scaling coefficient. This coefficient can be found in look-up tables or defined by the inverse of the Kolmogorov distribution at  $\alpha$ .

If the null hypothesis that the distributions are from the same distribution is not rejected, the least damaging cycle is deleted and the statistical test is again performed on the original baseline sample and the new sample with two missing cycle. This process is repeated until the null hypothesis is rejected. Since this process can be computationally expensive based on the length of the history and the number of cycles to delete, this search may be optimized using a binary search algorithm rather than evaluating cycles in order.

## 4.2 History Reconstruction

After the list of cycles has been reduced, the original load history can be approximately reconstructed. Using the information about when the extremes of each cycle occurred (using the range, mean, half cycle start times and half cycle time lengths), the points of the original history can be layered onto a history and connected to form a reduced history. This can be advantageous in condensing a history into a time series history containing only information relevant to the thermal cycling damage. This could be useful in planning an irregular load cycling test, so that the life can be simulated faithfully while minimizing the number of reversals that need to be programmed and executed. Figure 30 below is a portion of a reconstructed history superposed on top of the original portion of the outdoor dataset to illustrate the reduction in number of reversals.

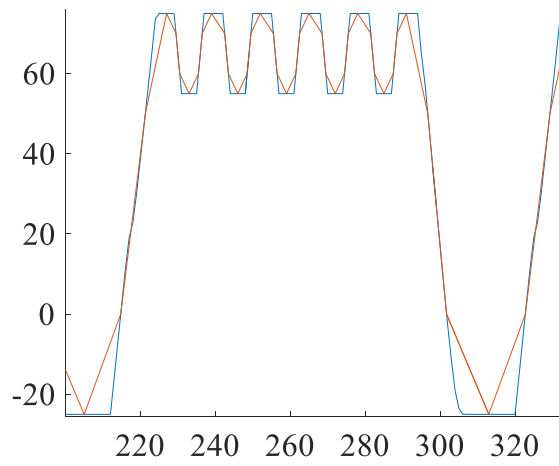
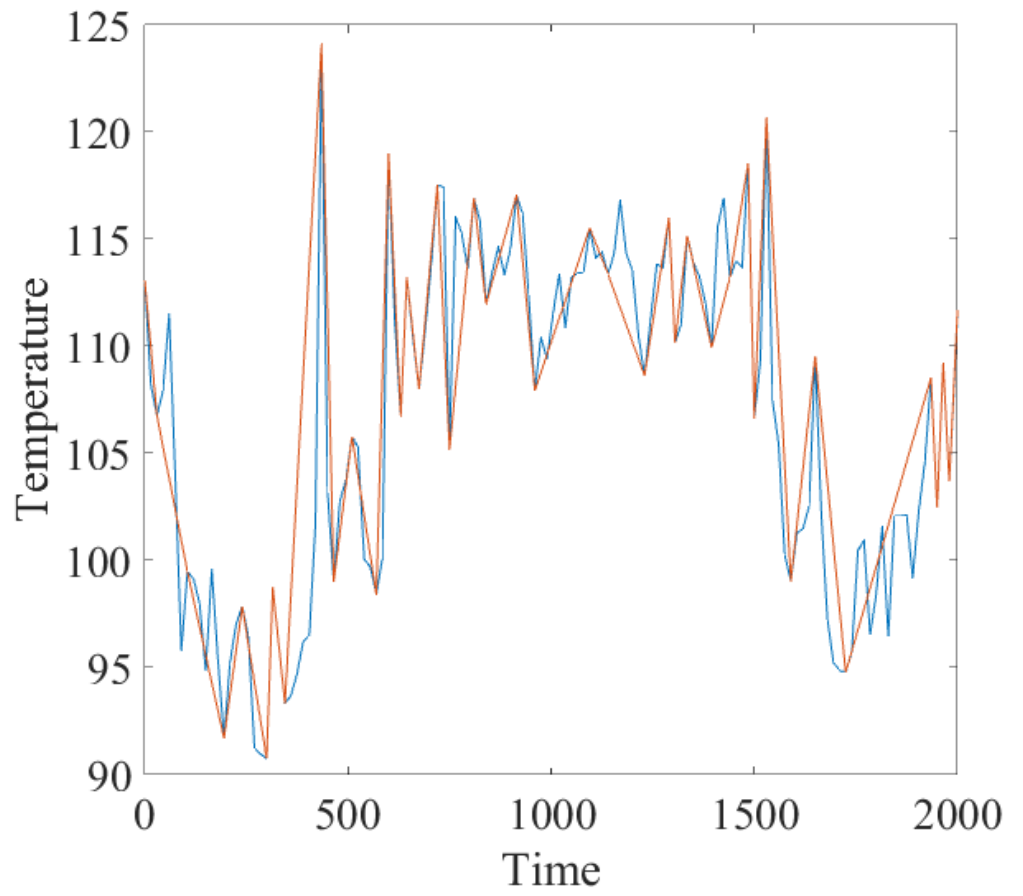


**Figure 30: Example of reconstructed history for outdoor data set (top) and test profile data set (bottom)**

### **4.3 Demonstration of Automated Cycle Reduction and Reconstruction**

The automated cycle reduction algorithm was executed on three test datasets (the test profile dataset did not have enough variation in types of cycles experienced to appreciably benefit from this cycle reduction) to demonstrate the performance (in terms of data reduction) of the approach. Each of the plots below (Figures 31-33) shows the percent reductions in points in the damage estimate (in blue), the number of half cycles from the cycle list resulting from rainflow counting, and the number of data points in the temperature history. The monotonic data was not retained in the reconstructed history, only the reversals. Each of the three reductions are plotted over a range of load range threshold percentage to evaluate the stability of the data reduction as a function of the user's choice in this input parameter.

All three datasets had an extremely small change in damage estimate as a result of the cycle reduction. This implies that the choice of test is cautious in terms of damage reduction. However, all three datasets had large reductions in both number of cycles retained and points in the temperature history. While in the outdoor and desktop datasets, the cycle lists were approximately cut in half, the laptop dataset experienced close to a 90% reduction in number of half cycles retained. Higher reductions were recorded in the length of reconstructed histories, but this result is padded by the fact that monotonic data was not retained.

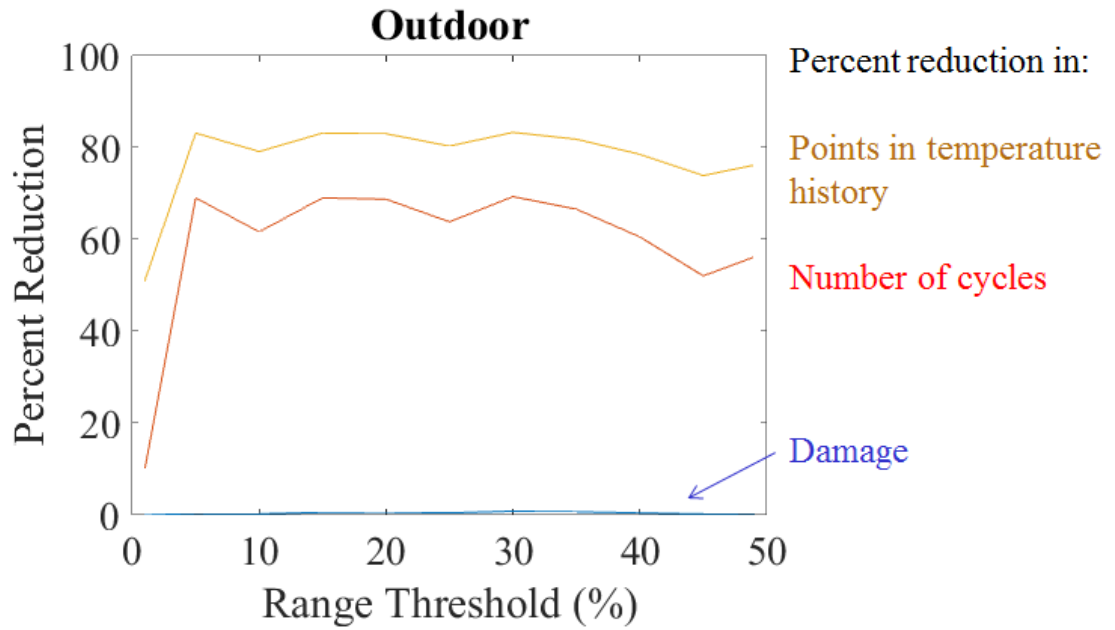


Figure 31: Data reduction for outdoor data set

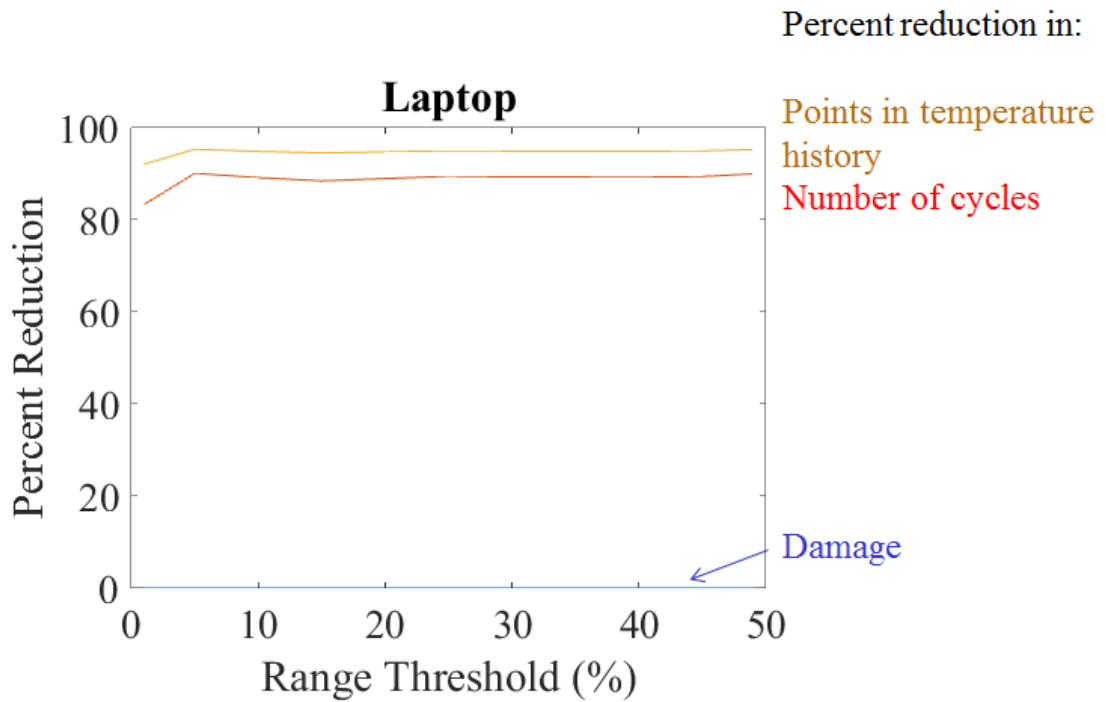
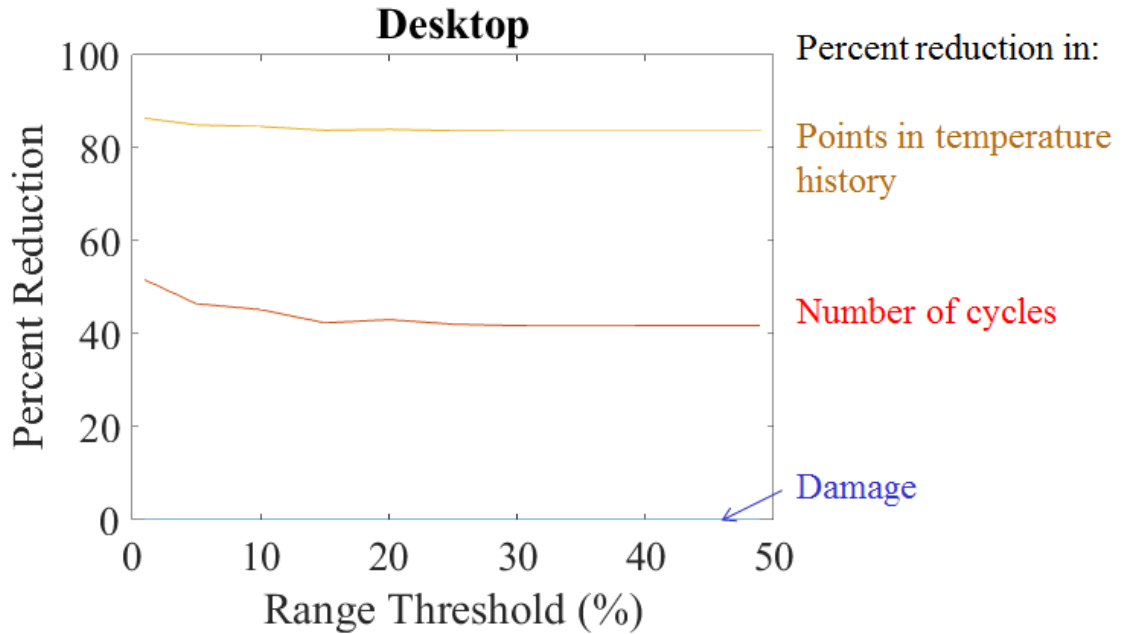


Figure 32: Data reduction for laptop data set



**Figure 33: Data reduction for desktop data set**

If it were assumed that these datasets extended to be a year a long at the same sampling rate, and that cycles were extracted at the same rate (extracted cycles per unit time index of the history) and the reduction in cycles and reconstructed history points were constant, it could be quantified how much data is saved in a year's worth of history.

Table 5 assumed that each point in the history features two numbers (time and load) stored in 8 bytes each, and each half cycle is extracted into 6 parameters (range, mean, upper dwell, ramp time, lower dwell and start time) in 8 bytes each. While the savings in terms of megabytes are modest (since all data files were less than a gigabyte to begin with) in applications where storage space is ample, this technique does allow sampling rates to be increased substantially to account for fast-changing loads, which otherwise would have filled a storage medium prohibitively fast. This could be useful especially combined with a line-fitting data reduction method such as the Ramer-Douglas-Peucker algorithm to reduce the size of the original time series history.

**Table 5: Data reduction comparisons**

|         | Cycle list |         | History  |           |    |
|---------|------------|---------|----------|-----------|----|
|         | Original   | Reduced | Original | Reconstr. |    |
| Outdoor | 916        | 331     | 561      | 110       | kb |
| Laptop  | 716        | 75      | 505      | 25        | mb |
| Desktop | 7.09       | 4.11    | 8.41     | 1.37      | mb |

## **5. Conclusions**

A multi-parameter rainflow algorithm which deletes, rather than retains, monotonic data between reversals will run faster than if dwell times are interpolated. However, in datasets where the load frequently varies non-linearly between reversals, the two approaches to dwell time estimation produce much different damage predictions. In this case, it may be advantageous to use the slower algorithm that estimates dwell time using more of the available information.

Using a supplementary algorithm to estimate dwell time is only applicable if the damage model of choice does not require dwell times to be defined within a particular extracted cycle. For example, if dwell damage and cyclic damage were calculated as summed independently, then this approach may be ideal since counting dwell regions and cycle extraction without interpolating dwells can be implemented in relatively fast algorithms (compared to cycle extraction with dwell interpolations). However, if dwells need to be defined for every extracted range, then this approach is unsuitable because it is definition dwell time improperly. If the counted dwell regions are used to estimate a probability distribution to be sampled at a one-to-one ratio with ranges and means during a probabilistic damage simulation, then an unrealistic situation is being simulated, since

the dwells have no connection to ranges. The resulting probability distribution would be artificial as a consequence.

In some mechanisms, such as fatigue, hysteresis loops in stress-strain space need to intersect, and therefore time removal may be unsuitable. Enabling time removal shrinks the area of the resulting half-cycles. Since the fatigue damage is related to the area of the cyclic hysteresis loop, using time removal makes the damage estimate smaller.

If a damage model that can be quickly iterated is available (e.g., does not require an excessive amount of computational time), damage reduction-based data reduction strategy can achieve large data reduction percentages. Reductions of about 90% were observed in some cases without appreciably impacting the damage estimate. The fact that this process is automated and non-parametric (i.e., does not require the user to specify an acceptable error tolerance parameter) increases the each of use.

## **5.1 Contributions**

This thesis developed a multi-parameter rainflow counting algorithm to estimate dwell time using monotonic data and retain cycle timestamps. This allows more of the available information to be used during damage estimates when dwell time are required to be defined within a particular extracted cycle, whereas this information was previously discarded prior to analysis

An automated data reduction algorithm was also developed to remove low-damage cycles and construct a simplified time-temperature history. Previous strategies either unacceptable altered the damage estimate of the analysis after reduction, or

required the user to choose an acceptable damage level. This method is non-parametric, so a user does not need to specify such an acceptable error.

## **5.2 Suggested Future Work**

While time removal seems to be disadvantageous based on the large reduction in damage estimates compared to not using time removal, it would make the analysis result in more aggressive (i.e. predicting later failures) life predictions. Since it is potentially such a large change, experimental evidence must be provided in order to justify its use.

Another useful avenue to explore would be the development of optimal binwidth and bandwidth formulas for non-parametric estimation of highly skewed distributions. Sample dwell time populations resulting from rainflow counting tended to have higher densities at lower values. Existing optimal binwidth formulas distorted probabilistic damage estimates as a result of over-coarsening the bins at low values, where most of the density lies. In other words, too much deference is given to high extremes and too little is given to small values. A non-linear binning rule may solve this.

## Works Cited

- [1] N. E. Dowling, "Fatigue in materials: introduction and stress-based approach," in *Mechanical Behavior of Materials*, Upper Saddle River, NJ, Pearson Prentice Hall, 2007, pp. 446-447.
- [2] ASTM International, "ASTM E1049-85: Standard Practices for Cycle Counting in Fatigue Practices," West Conshohocken, 2011.
- [3] C. Amzallag, J. Gerey, J. Robert and J. Bahuaud, "Standardization of the rainflow counting method for fatigue analysis," *International Journal of Fatigue*, vol. 16, no. 4, pp. 287-293, 1993.
- [4] C. McInnes and P. Meehan, "Equivalence of four-point and three-point rainflow cycle counting algorithms," *International Journal of Fatigue*, vol. 30, no. 3, pp. 547-559, 2008.
- [5] S. Downing and D. Socie, "Simple rainflow counting algorithms," *International Journal of Fatigue*, vol. 4, no. 1, pp. 31-40, 1982.
- [6] G. Glinka and J. Kam, "Rainflow counting algorithm for very long stress histories," *International Journal of Fatigue*, vol. 9, no. 4, pp. 223-228, 1987.
- [7] IPC, "IPC-SM-785: Guidelines for Accelerated Reliability Testing of Surface Mount Solder Attachments," Northbrook, 1992.

- [8] W. Engelmaier, "Fatigue of leadless chip carrier solder joints during power cycling," *IEEE Transactions on Components, Hybrids, and Manufacturing Technology*, vol. 6, no. 3, pp. 232-237, September 1983.
- [9] IPC, *Design Guidelines for Reliable Surface Mount Technology Printed Board Assemblies*, Northbrook, Illinois: IPC, 1996.
- [10] W. Engelmaier, "Soldering and mounting technology: performance considerations," in *Electronic materials handbook: packaging*, vol. 1, Materials Park, Ohio: ASM International, 1989.
- [11] W. Engelmaier and A. I. Attarwala, "Surface-mount Attachment Reliability of Clip-leaded Ceramic Chip Carriers on FR-4 Circuit Boards," *IEEE Transactions on Components, Hybrids Manufacturing Technology*, vol. 12, no. 2, p. 284, 1989.
- [12] W. Engelmaier, "Solder Joints in Electronics: Design for Reliability," in *TMS Annual Meeting Design of Reliable Solders & Solder Interconnections*, 1997.
- [13] W. Engelmaier, "The Use Environments of Electronic Assemblies and Their Impact of Surface Mount Solder Attachment Reliability," *IEEE Transactions on Component Hybrids Manufacturing Technology*, vol. 13, no. 4, pp. 903-908, 1990.
- [14] J. W. Evans, J. Y. Evans, A. Ghaffarian, K. Lee and C. Shin, "Simulation of Fatigue Distributions for Ball Grid Arrays by the Monte Carlo Method," *Microelectronics Reliability*, vol. 40, pp. 1147-1155, 2000.

- [15] H. Wei and K. Wang, "A probabilistic approach to predict thermal fatigue life for ball grid array solder joints," *Journal of Electronic Materials*, pp. 2314-2319, 2011.
- [16] N. Vichare, P. Rodgers and M. Pecht, "Methods for Binning and Density Estimation of Load Parameters for Prognostics and Health Management," *International Journal of Performability Engineering*, pp. 149-161, 2006.
- [17] M. Jones, "Simple boundary correction for kernel density estimation," *Statistics and Computing*, vol. 3, no. 3, pp. 135-146, 1993.
- [18] D. Scott, "On Optimal and Data Based Histograms," *Biometrika*, pp. 605-610, 1979.
- [19] D. P. Freedman and P. Diaconis, "On Maximum Deviation Between the Histogram and Underlying Density," *Zeitschrift für Wahrscheinlichkeitstheorie und verwandte Gebiete*, 58, pp. 139-167, 1981.
- [20] D. Vose, *Quantitative risk analysis*, Chichester, NY: Wiley, 1996.
- [21] R. Iman and W. J. Conover, "A Distribution-free approach to inducing rank correlation among input variables," *Communications in Statistics-simulation and Computation*, pp. 311-334, 1982.
- [22] A. Der Kiureghian and P. Liu, "Structural reliability under incomplete probability information," *Journal of Engineering Mechanics*, vol. 112, no. 1, pp. 85-104, 1986.

- [23] R. T. Clemen and T. Reilly, "Correlations and copulas for decision and risk analysis," *Management Science*, pp. 208-224, 1999.
- [24] G. R. MacKenzie, *Approximately maximum-entropy multivariate distributions with specified marginals and pairwise correlations*, Ph.D. Dissertation, University of Oregon, 1994.
- [25] F. Chai, "Solder Interconnect Life Prediction Under Complex Temperature Cycling With Varying Mean and Amplitude," University of Maryland, College Park, 2013.
- [26] K. D. Cluff, D. Robbins, T. Edwards and B. Barker, "Characterizing the commercial avionics thermal environment for field reliability assessment," *Journal of the Institute of Environmental Sciences*, vol. 40, no. 4, pp. 22-28, July 1997.
- [27] M. Denk and M. Bakran, "Comparison of counting algorithms and empirical lifetime models to analyze the load-profiles of IGBT power module in a hybrid car," in *Electric Drives Production Conference (EDPC), 2013 3rd International* , Nuremberg, 2013.
- [28] M. Nagode and M. Hack, "An online algorithm for temperature influenced fatigue life estimation: stress-life approach," *International Journal of Fatigue*, vol. 26, no. 2, pp. 163-171, February 2004.
- [29] N. Vichare, "Prognostics and health management of electronics by utilizing environmental and usage loads," 2006.

- [30] F. Chai, M. Osterman and M. Pecht, "Strain-Range-Based Solder Life Predictions Under Temperature Cycling With Varying Amplitude and Mean," *IEEE Transactions on Device and Materials Reliability*, vol. 14, no. 1, pp. 351-357, 2014.
- [31] D. H. Douglas and T. K. Peucker, "Algorithms for the reduction of the number of points required to represent a digitized line or its caricature," *Cartographica: The International Journal for Geographic Information and Geovisualization*, vol. 10, no. 2, pp. 112-122, 1973.
- [32] U. Ramer., "An iterative procedure for the polygonal approximation of plane curves," *Computer Graphics and Image Processing*, vol. 1, no. 3, pp. 244-256, 1972.
- [33] D. K. Prasad, S. Cho and M. Leung, "A parameter independent line fitting method," in *The First Asian Conference on Pattern Recognition*, Beijing, 2011.
- [34] H. Fuchs, D. Nelson, M. Burke and T. Toomay, "Shortcuts in Cumulative Damage Analysis," SAE Technical Paper 730565, New York, 1973.
- [35] JEDEC, "Temperature Cycling," JEDEC Solid State Technology Association, Arlington, 2014.
- [36] F. Chai, "Solder interconnect life prediction under complex temperature cycling with varying mean and amplitude," College Park, 2013.

- [37] W. Engelmaier, "Fatigue of Leadless Chip Carrier Solder Joints During Power Cycling," *IEEE Transactions on Components, Hybrids, and Manufacturing Technology*, vol. CHMT-6, no. 3, pp. 232-237, 1983.
- [38] P. P. Milella, "Damage Progression and Accumulation," in *Fatigue and Corrosion in Metals*, New York, Springer, 2013, p. 421.
- [39] H. J. Grover, *Fatigue of Aircraft Structures*, Naval Air Systems Command, 1966.
- [40] S. S. Manson, A. J. Nachtigall and J. C. Freche, *ASTM STP 415: Fatigue Crack Propagation*, Philadelphia: American Society for Testing and Materials, 1967.
- [41] ASTM International, "ASTM E1049-85: Standard practices for cycle counting in fatigue practices," West Conshohocken, 2011.